Instrument Data Metrics Evaluator for Tradespace Analysis of Earth Observing Constellations

Vinay Ravindra
Bay Area Environmental Research Institute
NASA Ames Research Center
Moffett Field, CA 94035
vinay.ravindra@nasa.gov

Sreeja Nag
Bay Area Environmental Research Institute
NASA Ames Research Center
Moffett Field, CA 94035
sreeja.nag@nasa.gov

***Abstract*— There is currently a trend towards developing and commissioning satellite constellation missions, which has necessitated tradespace studies to design high-performance, low cost and low risk constellations. An open-source software tool called Tradespace Analysis Tool for Constellations (TAT-C) has been developed at the NASA Goddard Space Flight Center, which aims to facilitate pre-phase A mission studies by generating and optimizing the tradespace of the constellations, involving a multitude of possibly coupled parameters such as orbits, satellites, launchers, ground-stations, and instruments. The performance attributes investigated by TAT-C are instrument data metrics, coverage metrics, cost and risk. While previous research has explored optimization of the constellation satellite orbits using metrics associated with coverage (such as maximizing access duration, maximizing the number of revisits over a region), there is relatively less work on exploring the tradespace of instrument parameters and associated data metrics. Previous research has also used relatively rudimentary data-metrics such as imaged pixel resolutions, range, and angles at which observations are made. This paper describes the instrument data-metrics evaluator of TAT-C which generates more sophisticated data metrics characteristic of the instrument type. The basic concept and the architecture of the evaluator have been developed to accommodate instruments without assuming specifics about the underlying technology. In this paper, we describe the modeling of the two most common types of Earth Observing instruments, namely passive optical sensors and synthetic aperture radars (SARs). The models allow for evaluation of commonly used data-metrics such as the signal to noise ratio, noise equivalent delta temperature, ground-pixel resolutions, dynamic range, noise-equivalent sigma0, etc. The challenges in making the models generic enough for wide usage, while being able to appropriately mimic characteristics of complex real-world instruments, are described using examples such as the Landsat-8 Thermal Infrared Sensor and Operational Land Imager. Lastly, we present results from the instrument data metrics evaluator for three important use cases of mission design with passive-optical sensors and SARs. The first use case explores the tradespace of Sun-Synchronous Orbits from a perspective of data-metrics as opposed to commonly considered coverage metrics. The second use case explores the tradespace of SAR parameters and highlights quantitative trade-offs between instrument parameters influencing the performance, size, and complexity. Such tradespace analysis allows the user to appreciate and consider a fundamental constraint on the SAR antenna size depending on radar frequency. In the last use case, we explore the tradespace of pushbroom vs whiskbroom scanners, and evaluate the conditions under which their performance match.**

TABLE OF CONTENTS

978-1-7281-2734-7/20/$31.00

1. INTRODUCTION

There are currently several efforts geared towards developing and commissioning satellite constellation missions in the Low Earth Orbit (LEO) for different applications. For example, companies like Axelspace and Planet [1] seek to provide frequent global imagery at visible, near-visible spectrum. Synspective [2], IceEye and Capella Space seek to provide frequent global radar imagery at microwave frequencies. SpaceX, OneWeb and Telesat are working to establish a global satellite broadband network for global internet services [3]. A common design element in all these efforts is the use of numerous (20's to 1000's) satellites in LEO to achieve (near) ubiquitous access globally.

Designing satellite constellations entail many design options, each design option with its own inherent risk, cost and reward. The design space of constellation missions is huge and there is an interest, and an immediate practical need to study the design space in an efficient manner, and understand the options and the trade-offs. As a practical example, consider the variety of design approaches taken by the above quoted companies which share similar goals. While Axelspace works with 100 kg class satellites, Planet works with Cubesats [1]. While SpaceX has planned for 4425 satellites in the constellation, OneWeb has planned for 720 satellites [3]. There is an obvious motivation to find an Pareto optimal design point to commission the mission. These factors motivated the development of the Tradespace Analysis Tool for Constellations (TAT-C) introduced in [4] [5], a tool to facilitate Pre-Phase A studies of remote sensing constellation missions in Earth orbit.

A key requirement of a tradespace analysis tool is the ability to quantify a constellation's performance, to compare different options available and weed out inferior designs. Traditionally, the emphasis of evaluating constellations has been in terms of the coverage related metrics such as revisit time, time to coverage, access time and area covered. Recent examples

include the works in [6] [7] [8] [9]. A single Low Earth Orbit (LEO) satellite has limited spatial coverage and revisit frequency, and hence there is the need to proceed towards a constellation of numerous LEO satellites. Quantifying the spatial and temporal characteristics of the constellation and using them to evaluate a constellation performance thus becomes important and motivated the works quoted above.

In addition to coverage related metrics, we emphasize that metrics related to the instrument data delivered by the constellation are also very important, because it represents the end product of a remote sensing constellation mission. The quality of the science data is hence another (along with coverage) indicator of a constellation's performance and should be considered in its evaluation. Loosely speaking, for a given set of resources (satellites and instruments), there is a negative correlation between coverage performance and data quality. As a simple example, consider a comparison between the extremes, a constellation architecture with Geosynchronous Earth Orbit (GEO) satellites and another with LEO satellites. A GEO constellation provides excellent coverage performance, and is capable of continuous near-global coverage with about just three satellites. However, the imagery provided by GEO constellations are of much coarser resolution (a data metric) as compared to the imagery provided by LEO constellations. In the telecommunication applications too, GEO suffers from high communication data latency relative to LEO.

Thus, consideration of the instrument data metrics along with coverage metrics is crucial to get a complete picture of the constellation performance. This paper describes an instrument data metrics evaluator and its contribution to tradespace analysis in Pre Phase A. While it was developed under the TAT-C framework, it can interface with any constellation evaluation and optimization tool. We outline several subtleties and considerations in the development of such a data metric evaluator. The paper is arranged as follows. In Section 2 we describe the concept of the evaluator. Section 3, Section 4 and Section 5 detail the modeling of three common instrument classes: a basic sensor class, passive optical sensor class, and the synthetic aperture radar class. In Section 6, we illustrate the tradespace analysis of representative and interesting case studies informed by the data metric evaluator. We summarize our conclusions in Section 7 .

2. Data Metrics Evaluator Concept

We introduce the framework of the data-metric evaluator for tradespace analysis in this section. Preliminary work on the same has been presented in [10]. Similar to the evaluation of coverage metrics in Wertz [11, 7.2], the data-metrics may be evaluated via two different approaches: (1) using analytic approximations or (2) using numerical simulations. In the analytic approach for coverage metrics evaluation, several approximations are made such as orbits approximated to be circular, ignoring rotation of Earth, etc. Instead of an analytic approach with such approximations, which may not bode well for all orbit configurations (such as elliptical orbits), we adopt a numerical approach for the data-metric evaluator.

A high-level functionality diagram of the data metrics evaluation of a single observation is shown in Fig.1. The inputs into the evaluator are described below, followed by description of the processing blocks indicated in the figure.

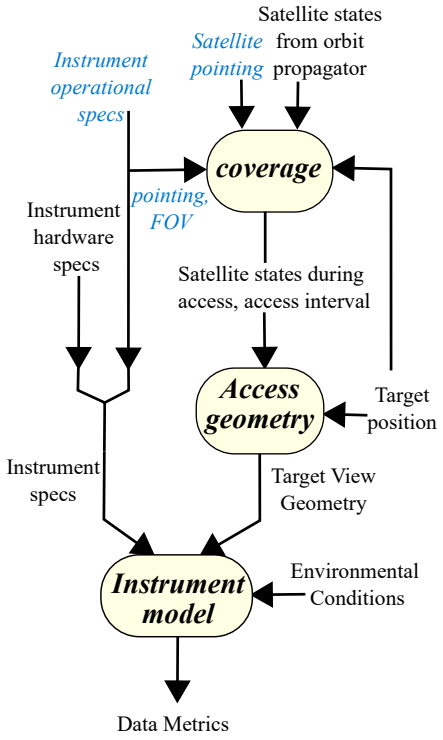

Figure 1: High-level block diagram of data-metrics estimation of an observation of a target point. The parameters in blue-italics are operational parameters.

1. *Satellite states:* The satellite state refers to the time-varying state of a satellite in the constellation containing the satellite's position and velocity vectors. It can be calculated using a numerical orbital propagation model [12], given the initial orbital state of the satellite. Appropriate care must be taken to account for effects of orbit maneuvering and station keeping during the orbit propagation. The access interval refers to the time interval during which the satellite "sees" the target.
2. *Satellite pointing:* The satellite pointing indicates the satellite orientation in Earth Fixed space, depending on the satellite attitude.
3. *Target position:* The "target" here refers to the object being observed, for example, land, sea, clouds, etc. The position is typically indicated in Earth-Fixed reference system in terms of latitude, longitude, altitude triplet. It may be noted that the target refers to a *single* point. The data-metrics calculated refer to the data-metrics of a single ground-pixel centered about the point.
4. *Instrument hardware specifications:* The term *hardware specifications* here is used to denote instrument parameters which are fixed during the mission. Examples of such parameters are focal plane array size of optical instruments and antenna size of radar instruments.
5. *Instrument operational specifications:* The term *operational specifications* here is used to denote variable parameters of instrument which can be configured during mission operations. Two of these specifications are indicated in the Fig.1 - instrument pointing and Field of View (FOV), which are necessary inputs for coverage calculations. They and some others are described below.

The instrument pointing is typically fixed with respect to the satellite pointing. In case of gimballed instruments, or instruments with electronic beam steering (such as in radars), the instrument pointing can be varied with respect to the satellite body frame during mission operations and captured

as a transfer function within the evaluator calculations.
The FOV is a solid angle (common shapes being conical and rectangular) centered around the instrument imaging axis, and observations are made of targets (land, sea, clouds, troposphere layer, etc) within this solid angle. While typically the FOV is fixed, in case of instruments like radars there are options for re-configuring the FOV using electronic beam forming.
Duty cycle maybe defined per orbit (ex: a 0.1 duty cycle implies the radar can be active only for 10% of the orbit period). Power hungry instruments such as radars are restricted to operate below a certain duty cycle. Instrument activity defines when the instrument is active (imaging), and when it is inactive

6. Environmental conditions: The celestial or atmospheric conditions during which the observation is made can greatly influence its quality. A simple example is the position of the Sun when an passive optical sensor makes observations. Observations cannot be made if access time corresponds to the local night time, and daytime observations may depend on the local solar time. Other examples are atmospheric conditions (clear, rain, fog, etc) which influence the magnitude of the electromagnetic energy falling on the instrument aperture. If there is prior knowledge of the target bi-directional reflectance distribution function (BRDF) and temperature, they too can be also be considered for higher fidelity of data metric evaluation. For example, the grassland areas can be assigned the BRDF of grasslands.

The satellite states from the orbit propagator, target position, satellite pointing, instrument pointing and the instrument FOV serve as inputs to the coverage calculations. The coverage calculations are done using *point coverage simulations* [11, 7.2.2] [12, Fig.3] after the numerical orbit propagation step. The region of interest to the mission is overlaid with a grid of ground points, and the *access* to each of these ground points is calculated. The data-metric evaluation too naturally follows into what may be termed as the *point data-metric simulations*. The *access* term used in this context refers to the event in which the target falls under the FOV of the instrument on-board the satellite. The output from the coverage calculations is the access interval and the satellite states during the access.

The process block labeled *Access geometry* takes as input the coverage output and the target position to compute the target view geometry. The target view geometry is calculated in terms of the observation angles, the observation range, Sun angles, etc. Note that this block depends on the instrument only in terms of the instrument pointing and the FOV (used in the coverage calculations), and is otherwise independent of the rest of the instrument parameters.

An *instrument model* process block maps the instrument specifications, target-view geometry and the environmental conditions to the data-metrics, by modeling the physics on which the instrument operates. For example, in the case of radar instruments, the physical principle is the radiation of electromagnetic energy from the instrument, followed by reception of echos from the target. The physical law governing this process of observation is the Radar equation, which would be modeled in this process block. Depending on the type of instrument, different data-metrics (such as σ_{NEZ0} for radars and SNR for optical sensors) are outputted. In this paper we describe the models of three types/ classes of instruments: basic-sensor, passive optical sensor and the synthetic aperture radar (SAR).

Issues for application in Pre-Phase A data metric evaluation

We encounter some issues when employing the above data-metric evaluation framework for Pre-Phase A mission analysis, as described below:

1. Issue introduced by operational parameters for data-metric evaluation: The operational specifications are by definition the parameters whose values are assigned during mission operation. Since they are not known during Pre-Phase A, the operational specifications to be used for the data-metric evaluation are uncertain.
As an example, consider the satellite and instrument pointing operational specifications. Agile pointing satellites have the ability to rapidly slew and make observations at different pointing angles. Typically, the maneuverability of the satellite is restricted to within a certain solid angle (ex: -30 deg $\leq$ roll $\leq$ +30 deg, -30 deg $\leq$ pitch $\leq$ +30 deg and corresponding yaw rotations to align one of the instrument axis along ground-track). Agile instruments can reorient their pointing (either mechanically or electronically) within the satellite and change their observation target without the need of satellite body maneuvering. Therefore, pre-defining satellite/instrument pointing for Pre-Phase A analysis is difficult.
One may use one of two approaches to deal with this issue. In the first approach one considers only the nominal pointing of both the satellite, instrument along with the nominal FOV of the instrument during the entire Pre-Phase A mission simulation. For example, typically the satellite body along with the instrument is aligned to the Local Vertical Local Horizontal (LVLH) frame. The instrument imaging axis points in the nadir direction (towards center of Earth) and the other axis of the instrument is aligned perpendicular to the ground-track. Another typical pointing is for the satellite to point perpendicular to the local land surface.
In the second approach one can use an arbitrary pointing axis and a solid angle centered around this axis spanning the entire region over which observations can be made. This solid angle is called as the Field Of Regard (FOR). The FOR differs from the FOV in that the FOV is the actual solid angle within which an image is taken (FOV $\leq$ FOR). In this approach all possible set of observations which can potentially be made are captured by the coverage calculator and later processed by to produce the data-metrics. However one should be cautious because in reality not all the observations captured by the FOR can be made.
Another example is the duty-cycle and the actual activation times of the instrument during the mission. These are operational specifications and are unknown at the Pre-Phase A stage. The simplest approximation would be to simply assume an instrument with 100% duty cycle and evaluate the data-metrics of all the possible set of observations during the mission. This can be done bearing in mind the simplification being made.

2. Issue of the unknown imaging instant: This issue relates to the previous issue on the unknown values of the operational parameters and needs an additional description. The actual imaging instant at which an observation is made is unknown at the Pre-Phase A stage. For example consider a Matrix imager (eg: a CCD camera) taking 2-dimensional images of land area as shown in Fig.2. In Case #1 the image is taken at time $t = 1$. Note the position of GP-1 and GP-2 when the image is taken. In Case #2 the image is taken at $t = 2$ and again note here that the relative positions of GP-1 and GP-2 w.r.t the satellite are different (as compared to Case #1). The data-metrics evaluated for a ground-pixel depends on the target geometry, and thus will yield different results depending on the time-instant of observation.

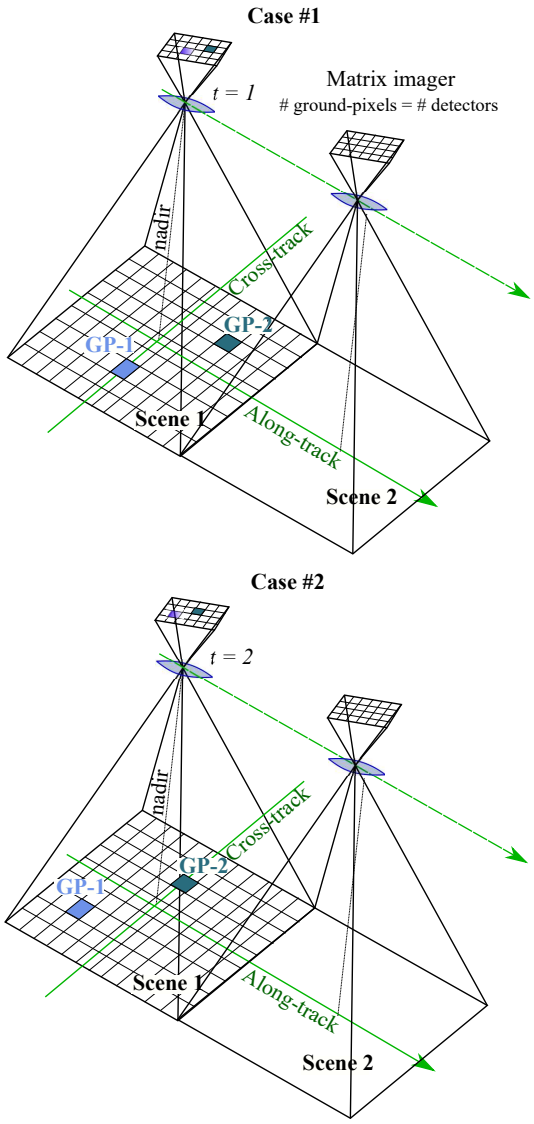

Figure 2: Illustration of imaging of 2D scenes by matrix imagers. Depending on the instant of imaging, the data-metrics of the individual ground-pixels may vary due to the different viewing geometries.

A simplification we make in this work is to calculate the data-metric of the pixel at the time-instant when the ground-point is seen at a purely side-looking angle (i.e. with no squint). For example, in Fig.2 the data metrics of GP-1 is evaluated at $t = 1$ and for GP-2 the data-metrics is evaluated at $t = 2$.

3. Issue of fidelity of instrument modeling: Real world satellite remote-sensing instruments are complex and unique. Modeling each instrument separately requires extensive effort and not only increases the complexity the underlying model, but also increases the complexity of the instrument input parameter space. In terms of application in Pre-Phase A studies the actual instrument technology maybe unknown and maybe very well be the answer we seek. Although in some cases it may be desirable to simulate the performance of existing instruments to get a measure of the relative performance with existing missions.
As an example consider the Landsat-8 Operational Land Imager (OLI) telescopic system which consists of four reflective

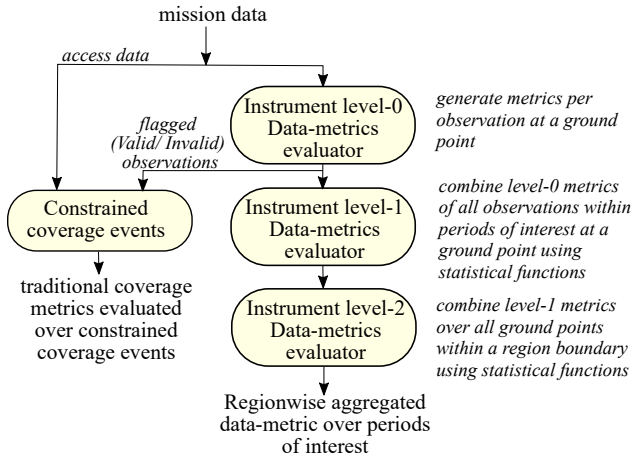

Figure 3: Block diagram of level-0, 1 and 2 metrics generation.

mirrors design [13] while the Thermal Infra Red Imager (TIRS) telescope consists of a compact four refractive lens design [14]. Both the instrument have similar operating principles and fall under the class of the passive-optical sensors (described in Section.4). An high fidelity approach of modeling would be model each of the telescopic systems along with separate instrument parameters for each of the elements of the telescope (example: spacing between the lens/ mirrors, lens/ mirror diameters, etc). Such an approach requires in-depth knowledge of the instrument technology (which in most cases is hardly available in open literature), and also makes the tool more complex for the person applying the data-metric evaluator for their Pre-Phase A studies.
The approach we take is to parameterize the physical operating laws of the instrument into a set of equivalent parameters of a predefined instrument model. For example, in the case of telescopic systems for optical instruments, we set the pre-defined model to be a single lens refractive system and while running evaluations of real-world instruments such as the OLI or TIRS, we find the equivalent set of parameters (such as the equivalent aperture diameter, focal-length) for this model. One of the challenge dealt in this work has been to find instrument models which can accommodate a variety of instruments sensibly.

Levels of Metrics

The data-metrics evaluated in Fig.1 are off a single observation at a ground-pixel centered about the target point. These are hereby termed as level-0 data metrics. Over the entire mission lifetime the level-0 data metrics are generated for numerous ground-points, and further in general, multiple observations per ground-point are possible over the course of mission. Thus we have huge volume of data-metrics at the end of evaluation of the mission.

The level-0 data metrics needs to be condensed into a smaller set so it can be used practically as a measure of the constellations performance. Fig.3 shows the block diagram of different levels of data-metrics generation. The level-1 metrics are generated for each ground point over periods of interest within the mission duration (eg: the month of July, or 2nd quarter of the year, or summer months of 3 years, etc) by aggregating the level-0 metrics of the ground point using statistical functions such as mean, variance, quantiles, etc. The level-1 metrics of each of the ground-points is then aggregated for all ground-points belonging to a region

(eg: the Western Ghats, the Himalayas, or the Sahara desert, etc), to generate the region-wise aggregated data-metrics over periods of interest.

A parallel-path in evaluation of *constrained coverage metrics* is seen in Fig.3. We define constrained coverage metrics as traditional coverage metrics (such as revisit time, percentage grid coverage), but evaluated over events which yield valid observations. As an example consider an passive optical sensor imaging at the visible (VIS) band. The access events from the coverage calculations may correspond to local night time conditions, when it is obvious that no valid observations can be made. In order to get "true/constrained" coverage the access events whose observations do not reach a threshold value of the data-metrics are filtered out and not considered in the coverage metrics calculations.

Fundamental Issues of the Evaluator Framework

As some final remarks in the this section, we observe that caution must be exercised while selecting the statistical functions for aggregating the level-0 metrics to the level-1/2 metrics. Quoting from [11, 7.2.2]: *"Statistical analysis of inherently non-statistical data, such as orbit coverage, can lead to dramatically incorrect conclusions."*, this remark applies to the case of statistical analysis of data-metrics as well.

Another caution which must be exercised is to bear in mind potential simplifications made using the *point data-metric evaluation*. In practice coverage calculations (and hence the following data-metric evaluations) are done with far-fewer grid points then what is is theoretically needed for accurate data-metric computations. As an example consider an instrument with typical pixel resolution of 100m x 100m. Suppose the region of interest for the mission is the entire Earth, in order to accurately calculate data-metrics over the entire region, a grid with $(\text{surface area of Earth})/100^2 = 51$Billion ground-points. Each of the ground-pixels potentially has different data-metrics associated with it due to different in viewing geometry, environmental conditions, etc. In our experience running coverage calculations and the data-metric evaluations for such a large number of ground points is time-consuming. Hence often the simulations are run with much smaller set of points and it is "hoped" that their distribution (with respect to the satellite ground-track) produces sufficient variety of samples of the data-metric distribution when simulated over a long mission duration. However there maybe some outlying cases where for example the satellite orbit is aligned with the ground point distribution, and can lead to biased results.

3. Basic Sensor Modeling

The purpose of the basic sensor class is to allow for obtaining primitive observation metrics in cases when there is incomplete information about the instrument specifications or when none of the existing instrument models can effectively account for the instrument functionality. This may be simply thought off as the *Geometry calcs* process block in Fig.1. Using the information about the satellite states and access interval given by the coverage module and the target geo-coordinates, the following four observation metrics relating to the target view geometry are calculated using simple vector geometry. Please refer to Fig.4. Unless indicated otherwise, all the position and velocity vectors are in the Earth-Centered-Earth-Fixed (ECEF) frame. Quantities in other frames of reference are indicated by a corresponding superscript.

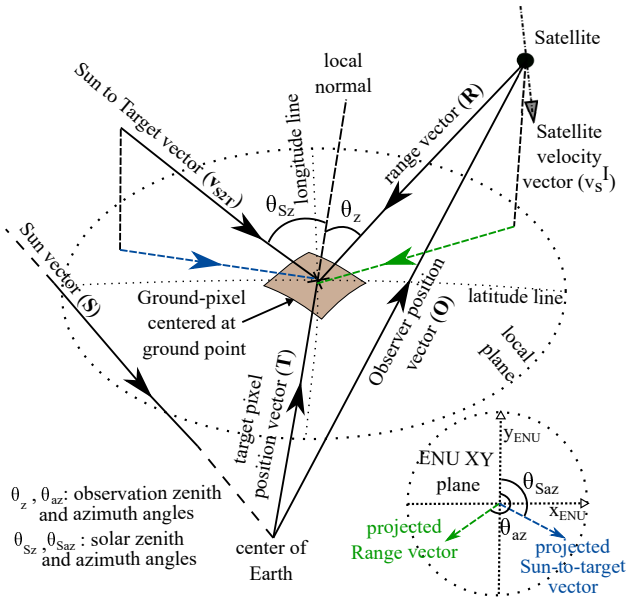

Figure 4: Basic sensor imaging geometry

Range ($\mathbf{R}$)

The range vector is the vector from the satellite to the point of observation. It can be calculated using:

$$\mathbf{R} = \mathbf{T} - \mathbf{O} \tag{1}$$

where $\mathbf{T}$ is the position vector to the point of observation (known from the geo-coordinates of the point) and $\mathbf{O}$ is the position vector to the satellite (observer) during access. The access interval is off non-zero length, and the position of the satellite considered in these equations corresponds to the instant when the satellite is "looking" at the ground-point at non-zero squint in a purely side-looking geometry (see Fig.2).

Observation zenith and azimuth angles (θ_z, θ_{az})

The observation zenith-angle (θ_z) is the angle between $-\mathbf{R}$ and the local normal vector $\mathbf{T}$. It is calculated as:

$$\theta_z = \arccos \frac{-\mathbf{R} \cdot \mathbf{T}}{\|-\mathbf{R} \cdot \mathbf{T}\|} \tag{2}$$

The calculation of the observation azimuth angle (θ_{az}) is performed by first transforming the observation range vector in the ECEF frame to the East-North-Up (ENU) frame defined at the ground point of interest to give $\mathbf{R}^{\mathbf{ENU}}$. The transformation from ENU to ECEF and vice versa can be done using the transformations given in [15, Appendix. C.3.6.3]. The azimuth angle is then the angle between the projection of $\mathbf{R}^{\mathbf{ENU}}$ in the XY plane of the ENU frame ($\mathbf{R}^{\mathbf{ENU}}_{\mathbf{XYproj}}$) and the unit y-axis vector of the ENU frame ($\hat{\mathbf{y}}^{\mathbf{ENU}}$, pointing to the North):

$$\theta_{az} = \arccos \frac{\mathbf{R}^{\mathbf{ENU}}_{\mathbf{XYproj}} \cdot \hat{\mathbf{y}}^{\mathbf{ENU}}}{\left\|\mathbf{R}^{\mathbf{ENU}}_{\mathbf{XYproj}}\right\|} \tag{3}$$

Sun zenith and azimuth angles ($\theta_{Sz}, \theta_{Saz}$)

The Sun zenith angle (θ_{Sz}) is an important quantity for passive instruments which rely upon Solar electromagnetic

energy for imaging. Together with the observation zenith angle the backscattered energy in the direction of the satellite can be determined. The calculation of θ_{Sz} is performed as follows:

1. *Calculate the Sun-to-Target vector:* The Sun vector depends on the date/time of observation and can be calculated in the ECI frame using the algorithm given in [16, Pg. 280]. The vector is then transformed into the ECEF frame using the Greenwich mean sidereal time of observation to give Sun vector in the ECEF frame $\mathbf{S}$. The transformation from a vector in the ECEF frame to the ECI frame (and vice-versa) can be done using the algorithm in [16, 1.6.1]. From $\mathbf{S}$ the Sun-to-target vector is calculated as $\mathbf{v_{S2T}} = \mathbf{S} - \mathbf{T}$.
2. *Determine if observation point in the Sun-lit side:* Depending on the observation time, the ground point maybe in the night-side. This can be verified by checking if a line-of-sight exists between the ground point and the Sun, or if it is eclipsed by Earth. The *LIGHT* routine algorithm in [16, Pg.198] can be used for this purpose.
3. Finally, if the ground point is in the Sun-lit side of Earth, the Solar zenith angle is calculated as the angle between the $\mathbf{T}$ and $-\mathbf{v_{S2T}}$:

$$\theta_{Sz} = \arccos \frac{-\mathbf{v_{S2T}} \cdot \mathbf{T}}{\|-\mathbf{v_{S2T}} \cdot \mathbf{T}\|} \tag{4}$$

The calculation of the Sun azimuth angle θ_{Saz} is performed by first transforming $\mathbf{v_{S2T}}$ in the ECEF frame to the ENU frame defined at the ground point of interest to give $\mathbf{v^{ENU}_{S2T}}$. The azimuth angle is then the angle between the projection of $\mathbf{v^{ENU}_{S2T}}$ in the XY plane of the ENU frame ($\mathbf{v^{ENU}_{S2T_{XYproj}}}$) and the unit y-axis vector of the ENU frame, $\hat{\mathbf{y}}^{\mathbf{ENU}}$

$$\theta_{Saz} = \arccos \frac{\mathbf{v^{ENU}_{S2T_{XYproj}}} \cdot \hat{\mathbf{y}}^{\mathbf{ENU}}}{\left\|\mathbf{v^{ENU}_{S2T_{XYproj}}}\right\|} \tag{5}$$

Radial relative speed (v_r^I)

The radial relative velocity (v_r^I, in the ECI frame) is an useful quantity in case of instruments (eg: synthetic aperture radars and Doppler radars) which take into advantage the high-relative velocity between the satellite and ground and make measurements of Doppler shifts in scattered electromagnetic waves to make observations. It can be calculated as follows:

1. *Calculate the velocity vector of the ground point in ECI frame:* The ground point has linear velocity ($\mathbf{v^I_{GP}}$) in the ECI frame due to Earth's rotation. The speed is constant and can be calculated from the angular speed of Earth and the radius of the smaller circle (formed by the latitude line) as follows:

$$v^I_{GP} = \omega_e \sqrt{(X^I_T)^2 + (Y^I_T)^2}$$

where ω_e is the angular rotation speed of Earth and X^I_T, Y^I_T are the x, y components of the Target vector in the ECI frame. The direction of the vector $\mathbf{v^I_{GP}}$ is calculated in the ECI frame by transforming the vector $[1, 0, 0]$ in the ENU frame (x-axis of the ENU frame pointing to the East) to the ECI frame and thus $\mathbf{v^I_{GP}}$ can be determined as:

$$\mathbf{v^I_{GP}} = v^I_{GP} ROT^{ECI}_{ENU} \hat{\mathbf{x}}_{\mathbf{ENU}} \tag{6}$$

where ROT^{ECI}_{ENU} is the rotation matrix to transform from the ENU frame to the ECI frame.

2. Calculate the relative velocity between the satellite and ground point as $\mathbf{v^I_s} - \mathbf{v^I_{GP}}$.
3. Finally the radial component of the relative velocity vector can be calculated as:

$$v^I_r = (\mathbf{v^I_s} - \mathbf{v^I_{GP}}) \cdot \frac{\mathbf{R^I}}{|\mathbf{R^I}|} \tag{7}$$

where $\mathbf{R^I}$ is the range vector $\mathbf{R}$ transformed from the ECEF frame to the ECI frame.

4. PASSIVE OPTICAL SENSOR MODELING

The framework of the passive optical sensors described here is based on the material in [11, Chapter 9]. This class of sensors encapsulates imagers which operate passively (i.e. the source of electromagnetic energy used for imaging is from external sources) in the optical and near-optical (IR and UV) spectra. Reference [11, Chapter 9] gives a complete description and example of data metric evaluation for a thermal whiskbroom-imager which uses the instrinsic radiation from Earth as the source of the electromagnetic energy. In this section we extend the treatment to include optical and near-optical (such as Short Wave Infra Red (SWIR)) spectra imagers whose source of electromagnetic energy is off the scattered reflections of Sun's energy from the Earths-surface/ atmosphere. Also some of the treatment as given in [11, Chapter 9] is tweaked to better model real-world instruments. In the rest section we detail the instrument model (see Fig.1) process block of the passive optical sensor class. First we lay out the instrument parameters followed by a detailed description of the model's physical laws leading to the calculation of the data-metrics.

The instrument parameters of a passive optical sensor class are outlined in Table 1, along with parameterized example real-world instruments: the Landsat 8 OLI, TIRS, the Terra/Aqua Moderate Resolution Imaging Spectroradiometer (MODIS) and an proof-of-concept design of a Cubesat Camera (CCAM).

Constraint conditions

Not all the passive optical instrument parameters listed in Table 1 are independent of each other. They are related by the following equations [11]:

$$\begin{aligned} \xi = \frac{d}{f} = \frac{\theta_{AT}}{N^{AT}_{pix}} = \frac{\theta_{CT}}{N^{CT}_{pix}} \\ F\# = \frac{f}{D_{ap}} \end{aligned} \tag{8}$$

where, ξ is the Instantaneous-FOV (IFOV, the field-of-view of a single detector), d is the (square) detector length, f is the focal length of the instrument, N^{AT}_{pix} and N^{CT}_{pix} are the number of ground-pixels in the along-track and cross-track direction respectively, $F\#$ is the F-number of the lens and D_{ap} is the aperture diameter. Note the distinction between *ground-pixels* and *detectors*. Detectors refer to the actual physical discrete sensing elements on the imaging aperture, while ground-pixels refer to the imaged pixels on the ground. Depending on the scanning method used, a single detector may image several ground pixels in a single scan. As an example of the real-world instruments satisfying the above quoted constraints consider the values of MODIS given in [23, Tabel 3]: focal-lengths (f) of 380.8mm and IFOV (ξ) of 0.354mr, 0.709mr and 1.418 mr, corresponding to detector sizes (d) of 135μm, 270μm and 540μm respectively.

Table 1: **Passive Optical Sensor parameters:** The passive optical sensor class is characterized into the parameters shown in the table. Note that the values shown for the example instruments correspond to only one particular band of operation of the instrument. Starred values are typical values from similar instruments.

Parameter	**TIRS Band-1** [14][17][18]	**OLI Blue-band**[19][13] [18]	**MODIS Band-10, Band-1** [11, 9.6.2] [20][21] [22][23]		**CCAM Blue band**[1] [24]
Orientation	Nadir-looking	Nadir-looking	Nadir-looking	Nadir-looking	Agile
Field of View ($\theta_{AT} \times \theta_{CT}$)[2]	141u^{r}x15^{o}	42.6u^{r}x15^{o}	141.8m^{r}x110^{o}	35.4m^{r}x110^{o}	1.2^{0}x1.2^{o}
Scan technique [3]	Pushbroom	Pushbroom	Whiskbroom	Whiskbroom	Matrix
Number of detectors[1]($N_d^{AT} \times N_d^{CT}$)	1x1850	1x6146	10x1	40x1	2048x2048
F-number ($F\#$)	1.64	6.4[4]	2.142	2.142	5.5
Focal Length (f)	178mm	845.1mm[4]	380.9mm	380.9mm	520mm
Operating wavelength (λ_0)	10.9um	482nm	490nm	645nm	470 nm
Bandwidth ($\Delta\lambda$)	0.6um	65nm	10nm	50nm	150nm
Photon to electron conversion efficiency (c_e)	2.5%	90% [4]	33*%	33*%	40%
Target black body temperature (T)	290K	290K	290K	290K	290K
Optics assembly efficiency (τ_{op})	60%[4]	90%[4]	80*%	80*%	60%
Bits per pixel	12	14	12	12	10*
Detector dimension (d)	25um	36um	540um	135um	5.5um
Aperture diameter (D_{ap})	108.5mm	132.0mm	177.8mm	177.8mm	94.6mm
Maximum detector integration time(T_i^{max})	3.49ms	3.6ms	323.3us	73.3us	678us
Number of read out noise electrons(N_r)	25*	8*	25*	25*	13

[1] Proof-of-Concept design

[2] Along-track direction x Cross-track direction

[3] Possible values are 'Pushbroom', 'Whiskbroom' and 'Matrix' imaging.

[4] From email conversation with Landsat 8 instrument scientist Philip W. Dabney.

Detector integration time calculations

The integration time of the detector depends on the access duration which the detector sees the ground-pixel. The total access duration which the instrument sees the ground-pixel is obtained from the coverage report (Fig.1). The duration to which the detector element is exposed to the electromagnetic energy from the ground-pixel depends on the scanning technique used, and the instrument electronics.

Before calculating the integration time, we first calculate the access duration's that the detector has for each ground-pixel. In case of pushbroom scanner and matrix imagers we have the access duration of the ground-pixel by a detector simply as:

$$A_{det} = A_{Ins} \tag{9}$$

where, A_{det} is the access duration of the ground-pixel by the detector, and A_{Ins} is the access duration of the instrument over the ground-pixel. A pushbroom scanner has effectively one row (perpendicular to the ground-track) of detector elements. The term "effective" is used because there may be multiple rows, the readings from which would be processed into a single-effective row. For example, in case of the TIRS we have two rows read out from each infrared band, and later combined by a ground-processing software into a single effective 1850-pixel row that has no inoperable pixels and covers the entire 185-km swath [14].

In case of Whiskbroom scanning we have possibly multiple detectors in the along-track direction (multiple rows, but only one column). The optical scanner splits the access time of the instrument to cover imaging of several cross-track ground-pixels. The integration time corresponding to a single ground-pixel scan is:

$$A_{det} = A_{Ins} \ \frac{N_{pix}^{AT}}{N_{pix}^{CT}} \tag{10}$$

The integration time will be typically less than the access duration since some time needs to allotted towards readout, and in some cases multiple samples may be taken over the available access duration. In [11] a simplification is made and the integration time is considered to be the access duration. However, in practice the sensor cannot continue to integrate with increasing integration time, and it reaches a saturation point. This is a problem in case of simulations applied to tradespace analysis, where we maybe searching over wide range of altitudes, and other parameters which may yield large instrument access duration. Hence we introduce another parameter called as the maximum integration time of detector elements *maximum detector integration time (T_i^{max})*. In this section we consider the integration time to be:

$$T_i = max(A_{det}, T_i^{max}) \tag{11}$$

where $max()$ is the maximum function and T_i is the integration time of the detector. To make the formulation more realistic we may further weigh down the A_{det} by a factor ≤ 1 so that time for charge readout and other electronic operations are allowed.

As an example consider the TIRS (pushbroom) parameters in [14][17]. The A_{Ins} for TIRS is 14ms corresponding to time taken to move over 100m (ground-pixel resolution) at a ground-speed of 7km/s. However the integration time is set to only 3.4ms corresponding to 25m image motion. One frame is produced every 0.014ms corresponding to the quoted 70 frames/s in [14][17]. Another example is the integration time of OLI (pushbroom) which is said to be commandable from 90us to 3600us [13]. The access duration calculated by taking the altitude of Landsat as 705km and the quoted pixel resolution of 30m (the 8 multispectral bands) gives the access duration of ground-pixel for a detector as 4.2ms ($\geq$3.6ms).

Radiance from Earth as black-body radiator

The unit of radiance we consider in the following discussion is [$photons\ s^{-1}m^{-2}sr^{-1}$]. Assuming that the Earth (target under observation) is a black-body and a Lambertian surface (obeying the Lambert's cosine law), we have the following intrinsic radiance from Earth (L_E) in the direction of the satellite from the target pixel:

$$L_E = \int_{\lambda_1}^{\lambda_2} L_\lambda(T)\tau_\lambda^{atm}(\theta_z)\cos(\theta_z)d\lambda \tag{12}$$

where, λ_1 and λ_2 are the lower and upper wavelengths of the band of interest respectively, θ_z is the observation zenith angle as defined in Section.3 and $\tau_\lambda^{atm}(\theta_z)$ is the spectral dependent atmospheric transmittance (function of the observation zenith angle), $L_\lambda(T)$ is the spectral radiance given from Plancks blackbody radiation equation as follows:

$$L_\lambda(T) = \frac{2h_P c^2}{\lambda^5}\frac{1}{e^{h_P c/\lambda k_B T} - 1} \tag{13}$$

where, h_P is the Planck's constant, c is the speed of light, λ is the wavelength at which the spectral radiance is calculated, k_B is Boltzmann's constant and T is the blackbody temperature of the target.

The atmospheric loss model considered in this paper is the LOWTRAN-7 model, which calculates atmospheric transmittance and background radiance for at given atmospheric path at low spectral resolution [25]. Implemented originally in FORTRAN, it has been available as an open-source lightweight python package (which acts as a wrapper to the original FORTRAN source code) at [26].

Radiance from Earth as reflector of Solar energy

The downwelling radiance from Sun (L_S^{dw}) onto the target pixel can be again calculated using Planck's spectral radiance from a blackbody at temperature of 6000K:

$$L_S^{dw} = \int_{\lambda_1}^{\lambda_2} L_\lambda(T_S)\tau_\lambda^{atm}(\theta_{Sz})\cos(\theta_{Sz})d\lambda \tag{14}$$

where, T_S is blackbody temperature of Sun (6000 K) and θ_{Sz} is the Solar zenith angle at the ground-pixel as defined in Section.3.

The area of the pixel (A_{gp}) can be calculated from the pixel resolutions (covered later in this section) as:

$$A_{gp} = \rho_{CT}\rho_{AT} \tag{15}$$

where ρ_{CT} is the cross-track pixel resolution and ρ_{AT} is the along-track pixel resolution.

The downwelling photon-rate (P_S^{dw}) (unit: photons/s) is then:

$$P_S^{dw} = L_S^{dw}A_{gp}\frac{\pi r_S^2}{|\mathbf{v_{S2T}}|^2} \tag{16}$$

where r_S is the Solar radius and $\mathbf{v_{S2T}} =$ is the vector from Sun to target ground point as calculated in Section 3.

Assuming unity reflectivity, the upwelling photon-rate (P_S^{uw}) due to scattering of the incident photons on the assumed Lambertian surface in the direction of the satellite is calculated as:

$$P_S^{uw} = P_S^{dw}\cos(\theta_z) \tag{17}$$

Finally we can calculate the upwelling radiance (L_S^{uw}) to the instrument as:

$$L_S^{uw} = \frac{P_S^{uw}}{4\pi A_{gp}} \tag{18}$$

Radiance to signal electrons calculation

The total radiance to the instrument is:

$$L = L_E + L_S^{uw} \tag{19}$$

The rate of photons radiated, reflected from the pixel is $P_{pix} = LA_{gp}$. From this we can calculate the rate of photons at the instrument aperture (P_{ap}) as:

$$P_{ap} = \frac{P_{pix}}{R^2}(\frac{D_{ap}}{2})^2\pi \tag{20}$$

where D_{ap} is the aperture diameter and R is the range from satellite to pixel as calculated in Section 3.

Considering the optical system losses we have the photon rate at the detector element (P_{det}) as:

$$P_{det} = P_{ap}\tau_{op} \tag{21}$$

where τ_{op} is the optical transmission factor.

The number of signal electrons collected (N_s) is then:

$$N_s = P_{det}T_i c_e \tag{22}$$

where c_e is the conversion-efficiency (i.e. the efficiency of conversion of incident photons to electrons) of the detector. This is similar to the quantum efficiency parameter used in [11, Chapter 9] and T_i is calculated from (11).

There are four data-metrics evaluated:

Signal-to-Noise Ratio (SNR)

The SNR is a measure of the radiometric performance of the instrument. Considering the shot noise ($\sqrt{N_s}$) and readout noise (N_r) as uncorrelated noise sources we can write the SNR as [11, Chapter 9]:

$$SNR = \frac{N_s}{\sqrt{N_s + N_r^2}} \tag{23}$$

Note that this SNR calculation assumes unity albedo. For an higher fidelity calculation one may introduce the more realistic albedo depending on imaging geo-coordinates (for ex: latitude = 0^o, longitude = 0^o falls in the Atlantic ocean where an low albedo may be assumed).

Noise-Equivalent-Delta-Temperature ($NEDT$)

The $NEDT$ characterizes the instrument in its ability to resolve temperature variations for a given background temperature (applicable to instruments operating in thermal bands) and can be calculated as [11, Chapter 9]:

$$NEDT = \frac{N_s(T)}{N_s(T + 1K) - N_s(T)} \tag{24}$$

where, $N_s(T)$ is the number of signal electrons calculated for a target temperature of T, and $N_s(T + 1)$ is the number of signal electrons calculated for target temperature of $T + 1$ Kelvin.

Table 2: **Typical values of the data-metrics of passive optical sensors:** See Table 1 for the corresponding instrument parameters. The data metrics are off a target pixel at the nadir.

Data Metric	**TIRS Band-1** [14, Fig.9] (705km altitude)	**OLI Blue band** [13, Table 1] [19, Table 4] (705km altitude)	**MODIS Band-10, Band-1** [23, Table 2] [20] (705km altitude)		**CCAM Blue band**[1] [24] (400km to 700km altitude)
Signal to Noise ratio (SNR)	10.8um: 390@240K, 2536@360K [2]	367 typical (on-orbit measured)	802 (requirement)	128 (requirement)	Typical: 20, High: 6800, Cloud: 13500
Noise-Equivalent Delta Temperature ($NEDT$)	10.8um:0.039@240K, 10.8um: 0.057@360K (on-ground testing)	*-NA-*	*-NA-*	*-NA-*	*-NA-*
Max Dynamic Range (DR_{max})	4096[3]	16384[3]	4096[3]	4096[3]	1039[4]
Resolution (ρ_{AT}, ρ_{CT}) at nadir	100m	30m	1000m	250m	5m

[1] Proof-of-Concept design
[2] Calculated from NEdL values as $SNR = L(\lambda)/NEDL$
[3] Calculated approximately as 2 power of number of bits per pixel
[4] Calculated as the ratio of maximum (Cloud) signal electrons to readout noise electrons

Dynamic Range

The dynamic range of the instrument also characterizes the radiometric performance of the instrument. It is the quotient of signal- and read-out noise electrons the sensor sees between dark and bright scenes at the given reflection coefficient of the target scene and can be estimated as [11, Chapter 9]:

$$DR = \frac{N_s}{N_r} \tag{25}$$

The signal levels in analog form are quantized to discrete levels. The maximum number of levels possible is given by $2^{\#\ bits\ per\ pixel}$. The number of bits per pixel should be greater than the maximum DR (corresponding to maximum number of signal electrons from the brightest target expected to be observed) so that all signal levels are captured without loss of information due to bit saturation.

Ground-pixel resolutions (ρ_{AT}, ρ_{CT})

The ground-pixel resolutions give measure of the spatial resolution of the observations made by the instrument. They can be be calculated from the IFOV (ξ) of the detector element as follows:

$$\rho_{AT} = \xi R \tag{26}$$

$$\rho_{CT} = \xi \frac{R}{\cos(\theta_z)} \tag{27}$$

where R is the range from satellite to ground point and θ_z is the observation-zenith angle as described in Section.3. These equations assume that the imaging geometry is purely side-looking with no squint (Fig.2).

To get some idea of the typical values for the data-metrics we have surveyed the measured/design-specified data-metric values for example instruments which is given in Table 2.

5. SYNTHETIC APERTURE RADAR MODELING

Synthetic Aperture Radar (SAR) is an active instrument operating in the microwave range of spectrum. A comprehensive review of the same can be found in [27], [28]. In general there are several imaging modes in SAR imaging such as the Stripmap mode, ScanSAR mode and Spotlight mode [28]. Here we consider the fundamental and commonly used SAR imaging mode, the 'Stripmap' mode which can be said is similar to the pushbroom scanning in passive optical sensors. The framework of synthetic aperture radar (SAR) described here is based on the material in [29] and [30].

The configurable parameters of SAR are listed in Table 3 along with the example values for SAR operating in the L-band, C-Band and X-band. The SAR data-metrics can be derived from these parameters and by making reasonable assumptions, the description of which is given in the rest of this section.

Field-of-View (FOV) calculations

SAR instruments commonly have rectangular planar-array antennas with the larger dimension aligned in the direction of the satellite motion. In radar terminology the along-track direction is also referred to as the azimuth direction and the dimensions of the antenna in the azimuth direction is denoted by D_{az}. The dimension of the antenna in the cross-track direction (also referred to as the elevation direction) is denoted by D_{elv}. The FOV of the SAR depends on the aperture excitation profile and the size of the antenna. Commonly the antenna designs involve having an uniform aperture excitation with some optional tapering at the edges of the antenna panel (to prevent having side-lobes which result in unwanted echo returns). By assuming an uniform aperture excitation, the FOV can be found by calculating the 3dB beamwidth of the antenna is the along-track (θ_{az}) and cross-track (θ_{elv}) directions as follows [29, eq.41]:

$$\theta_{az} = \frac{\lambda_0}{D_{az}}, \quad \theta_{elv} = \frac{\lambda_0}{D_{elv}} \tag{28}$$

Table 3: **Synthetic Aperture Radar parameters:** The synthetic aperture radar (SAR) class is parameterized as shown in the table. Also shown are example parameter values of different SARs. Starred values are typical values.

Parameter	**SeaSat-A L-band SAR** [31][30]	**ERS-1 C-band SAR** [30]	**MicroX-SAR X-band SAR** [32]
Orientation	Side-looking, 20.5°	Side-looking 20°	Side-looking 30°
Operating frequency (f_0)	1.2757GHz	5.25GHz	9.65GHz
Chirp Bandwidth (B_T)	19MHz	15.5MHz	75MHz
Antenna along-track dimension (D_{az})	10.7m	10m	4.9m
Antenna cross-track dimension (D_{elv})	2.16m	1m	0.7m
Antenna aperture efficiency (η_{ap})	0.6	0.26	0.5
Peak transmit power (P_T)	1kW	4.8kW	1kW
Transmit pulse-width (Δt_p)	33.4us	37.1us	31us∼83us
Minimum PRF (f_P^{max})	1463Hz	1680Hz	3000Hz
Maximum PRF (f_P^{min})	1640Hz	1700Hz	8000Hz
Scene noise temperature (T)	290K	290K	290K
System Noise Figure	5.11dB	3.4*dB	4.3dB
Radar losses	3.5*dB	3.5*dB	3.5dB
Bits per pixel	5	5	16

where, $\lambda_0 = c/f_0$ is the operating center wavelength (f_o is the operating center frequency, c here is the speed of light).

Pulse Repetition Frequency (PRF) constraints

There are four constraints imposed on the Pulse Repetition Frequency (PRF) which must be satisfied while making an observation. If these constraints are not satisfied, the instrument cannot make observations even if the target is within the FOV of the instrument. While the first two conditions impose outer bounds on the PRF, the next two conditions impose restrictions of PRF usage within the outer bounds.

1. The PRF should be high enough to allow for unambiguous sampling of the Doppler shifts in the return echo, and this condition gives the PRF_{min} as [29, Pg.27]:

$$PRF_{min} = Int(\frac{2v_s^I}{D_{az}}) \tag{29}$$

where $Int()$ is the integer function and v_s^I is the speed of the satellite in the ECI frame.
2. The length of the echo from the desired imaging swath (i.e. the swath illuminated by the main beam of the antenna) should be less than the inter-pulse period. This is to ensure the desired echo (either in whole or part) does not return when the radar is transmitting pulses. Refering the SAR imaging geometry in Fig.5 and [30, Pg.22 to 24] we have:

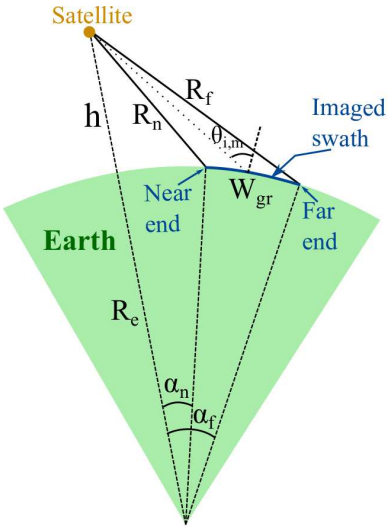

Figure 5: SAR imaging geometry. SAR is a side-looking instrument, and typically at a zero-squint angle (i.e. no pitch, only a non-zero roll). This orientation is necessary for unambiguous range measurements.

$$R_S = R_e + h$$
$$R_n = \sqrt{(R_e^2 + R_S^2 - 2R_eR_s\cos\alpha_n)}$$
$$R_f = \sqrt{(R_e^2 + R_S^2 - 2R_eR_s\cos\alpha_f)}$$
$$\tau_{near} = 2\frac{R_n}{c}, \quad \tau_{far} = 2\frac{R_f}{c}$$

$$PRF_{max} = Int(1/(2\Delta t_p + \tau_{far} - \tau_{near})) \tag{30}$$

where R_S is the distance to the satellite, R_e is the radius of Earth, h is the altitude of the satellite, R_n, R_f are the distances to near and far end of swath from satellite respectively, τ_{near}, τ_{far} are the time intervals from transmit of pulse to return of the echo to the SAR from the near and far end of the swath respectively, α_n, α_f are the Earth central angles to the near and far end of swath respectively, Δt_p is the radar pulse-width (an instrument parameter in Table 3) and PRF_{max} is the maximum PRF which can be used to obtain an observation. The *desired* imaging swath usually refers to the swath illuminated by the 3dB elevation beamwidth of the antenna. It may be made more narrower to accommodate higher PRFs.
3. The echos from the desired imaging swath do not overlap with a future transmit pulse. From [30, eq.5.1.4.1] we have the restricting condition of the PRF (f_P) as:

$$\frac{N-1}{\tau_{near} - \Delta t_p} < f_P < \frac{N}{\tau_{far} + \Delta t_p} \tag{31}$$

where, $N = Int(f_P\frac{2R_n}{c}) + 1$ is the (future) transmit pulse number (referenced to the pulse whose echo we are interested in avoiding eclipsing) just before which echo from the near end of the swath is received.
4. The final condition to be imposed on the PRF is that the echo from the desired region should not overlap with returns from the nadir. The antenna beam-pattern of any practical SAR will have numerous sidelobes (in directions outside the

Table 4: **Typical values of the data-metrics of synthetic aperture radars:** The values correspond to stripmap mode of the corresponding SAR (with parameters given in Table 3) and at the middle of swath.

Data Metric (mid-swath)	**SeaSat-A** [31] (800km altitude)	**ERS-1** (777km altitude) [30]	**MicroXSAR** [32] (600km altitude)
Sigma NEZ0 σ_{NEZ0}	-25dB	-24dB	-15dB
Resolution (ρ_{AT}, ρ_{CT})	25m	26m	3m
Incidence angle (θ_z)	23.2^o	23^o	33.2^o

main lobe(beam)). Thus a small fraction of the radar echo energy is transmitted and received at directions outside the main beam and this leads to echo returns from regions outside the desired swath region. Such returns degrade the observations and are especially strong at the nadir direction since the nadir corresponds to the shortest range from the satellite to Earth. The condition can be written as the following expression:

$$f_P \notin \left[\frac{m}{\frac{2R_n}{c} - \frac{2h}{c} - \Delta t_{nadir}}, \frac{m}{\frac{2R_f}{c} + \Delta t_p - \frac{2h}{c}} \right] \quad (32)$$

where, $\tau_{nadir} = 2h/c$ is the time interval from time of transmit of pulse to return of echo from the nadir, $1 \leq m \leq M$, where $M = Int(f_P \frac{2R_f}{c}) + 1$ is the (future) transmit pulse number (referenced to the pulse whose echo we are interested in avoiding eclipsing) after which echo from the far end of the swath shall be received. There is a mismatch in the corresponding expression for this condition given in [30, eq.5.1.5.2] versus ((32)). Hence a derivation of ((32)) is given in the Appendix A.

Figure 16 in the Appendix.A shows the tradespace plot of the PRF versus sidelook angle highlighting the regions of inoperable PRF. While the above four constraints impose fundamental limits on the PRF depending on the imaging geometry (altitude, look-angle), transmit pulse width and swath size, the instrument itself has one range of operable PRF given by $[f_P^{min}, f_P^{max}]$ (Table 3). The actual PRF used during imaging is an operations parameter. One may use the highest possible (satisfying all the constraints) PRF (f_P) within the range $[f_P^{min}, f_P^{max}]$ as the value of this parameter. This is a reasonable assumption since an higher PRF leads to an higher quality of image (due to higher average transmit power for fixed transmit pulse width [29, eq.17]).

There are three SAR data-metrics evaluated:

Noise Equivalent Sigma Zero (σ_{NEZ0})

The σ_{NEZ0} is the reflectivity of the target region which results in unity signal-to-noise ratio of the image. A lower σ_{NEZ0} is desired since it implies that for a given target reflectivity the sigma-to-noise ratio level is higher. From [29, eq.37] we have:

$$\sigma_{NEZ0} = \frac{265\pi^3 kT}{c} R^3 v_s^I \cos(\psi_g) \frac{B_T F_N L_{radar} L_{atmos}}{P_{avg} G_A^2 \lambda_0^3} \quad (33)$$

where T is the scene-noise temperature, B_T is the chirp-bandwidth, $\psi_g = \pi/2 - \theta_z$ is the grazing angle, $P_{avg} = \Delta t_p f_P P_T$ is the average transmit power, P_T is the peak-transmit power, $G_A = 4\pi \frac{\eta_{ap} D_{az} D_{elv}}{\lambda_0^2}$ is the gain of the SAR antenna (assuming uniform aperture excitation), η_{ap} is the antenna aperture efficiency, F_N is the system noise-figure, L_{radar} are the radar hardware related losses and L_{atmos} is the two way atmospheric-loss.

[29, eq.37] includes an additional term in the σ_{NEZ0} equation, $\frac{L_r L_a}{a_{wr} a_{wa}}$ which relates to signal-processing issues. However in the absence of more information the parameters a_{wa}, L_a, a_{wr}, L_r can each be set to 1.2 ([29, Pg.9,10]) and this term reduces to unity.

Observation zenith angle θ_z

The observation zenit -angle (θ_z) is popularly referred to as the incidence angle in SAR literature. Section.3 gives the formula for calculation of the incidence angle. Depending on the application certain incidence angles are more favorable. For example large incidence angles are more favorable for observing surface topography because of the resulting shadowing, while small incidence angles are desirable because of the high sensitivity of the surface direct backscatter coefficient to variations in the surface slope and intermediate incidence angles are favorable for observing surface roughness [33]. For an ambitious constellation application we may want acquisition of SAR images over range of incidence angles to get complete information about the target region.

Ground-pixel resolutions (ρ_{AT}, ρ_{CT})

The pixel resolutions for an SAR image unlike the case of passive optical sensors are independent of the observation range. From [29, eqns.23,36] we have the cross-track resolution (ρ_{CT}) as:

$$\rho_{CT} = \frac{a_{wr} c}{2 B_T \cos\psi_g} \quad (34)$$

where a_{wr} is a signal processing factor (range impulse response broadening factor due to data weighting or windowing) which has a typical value of 1.2.

The along-track resolution (ρ_{AT}) is [30, 5.3.6.3]:

$$\rho_{AT} = \frac{D_{az}}{2} \frac{v_g}{v_s^I} \quad (35)$$

where v_g is the ground speed of the satellite.

6. TRADESPACE STUDY EXAMPLES

This section describes examples of tradespace analysis carried out using the instrument data metric evaluator. There are three cases explored each with an unqiue attribute. In the first case the tradespace explores the variation in the data metrics with a single instrument over a search space of

different orbits. In the second case we consider a search space of multiple instruments (different instrument parameters) and evaluate it for a single orbit. Finally in the third case we explore a search space of different instrument technologies. The tradespace is evaluated over all possible combinations of the search space parameters to illustrate a potential trend. The evaluated trend is justified conceptually and also quantified.

Case 1

The example we consider in this case are off circular Sun-Synchronous Orbits (SSOs) which are designed to make observations at the same Mean Local Solar Time (MLST) at a place throughout the mission lifetime. SSOs are popular type of orbits used for remote-sensing missions which depend on energy from Sun for lighting the target due to the nearly same illumination conditions throughout the mission. SSOs also have the properties that it results in a nearly constant thermal environment due to the Sun exposure for the satellite remaining the same over the mission life [34] and that most Sun-synchronous missions have fairly constant eclipse periods and a smaller range of Sun angles to contend with, and have a "cold side" of the spacecraft that is never in direct sunlight [11, 11.5.5]. The last two properties help with thermal design of a spacecraft.

Reference [34] gives description about the design of SSOs. There is a fixed relationship between the altitude and inclination for a SSO of given eccentricity (see [34, Fig.2]). The design process begins by first selecting the orbit altitude, to ensure a desired ground-repeat-track period and spacing between adjacent ground-tracks (coverage metrics). Then the inclination is selected depending on the altitude and the SSO constraint, followed by selection of the orbit Right Ascension of Ascending Node (RAAN) (tied to the orbit epoch) depending on the MLST requirement at the orbit ascending node. This specification is commonly called as the Local (Mean Solar) Time at Ascending Node and is abbreviated as LTAN.

The motivation for the case study described in this section stemmed from the following two intuitions. Firstly, while an SSO is specified according to the MLST at the ascending node (on the equator), the MLST at the other latitudes is different depending on the inclination of the SSO. Thus for a mission designed to make observations over the entire globe or over regions distributed over the globe, the observations do not occur at the same MLST. Thus there is a spatial dependence on the expected observation data-metrics (eg. SNR) for an SSO orbit of specified LTAN. Given that the altitude of the SSO is constrained to be selected according to desirable coverage metrics, the inclination is automatically decided and hence there is no room to negotiate the distribution of the data-metric over the latitudes.

Secondly, while a SSO ensures the same MLST (mean Sun position) over the mission, the true local solar time (true Sun position) at which the observations occur for a latitude are different over the mission lifetime. The solar illumination at a latitude on the same MLST of each day varies over the year. The phenomenon of the true Solar time differing from the mean Solar time (MLST) is attributed to the ellipticity of the Earth's orbit around the Sun and the obliquity of the ecliptic. The difference in the Solar illumination is noticeable to a large degree at the higher latitudes (of both the hemispheres). As an extreme example consider the north polar region where there is constant sunshine during the entire summer while the vice-versa is true when during the winter after October there is constant darkness. A satellite in a SSO orbit regardless of the chosen LTAN would be able to take observations at both the ascending and descending passes (at the north

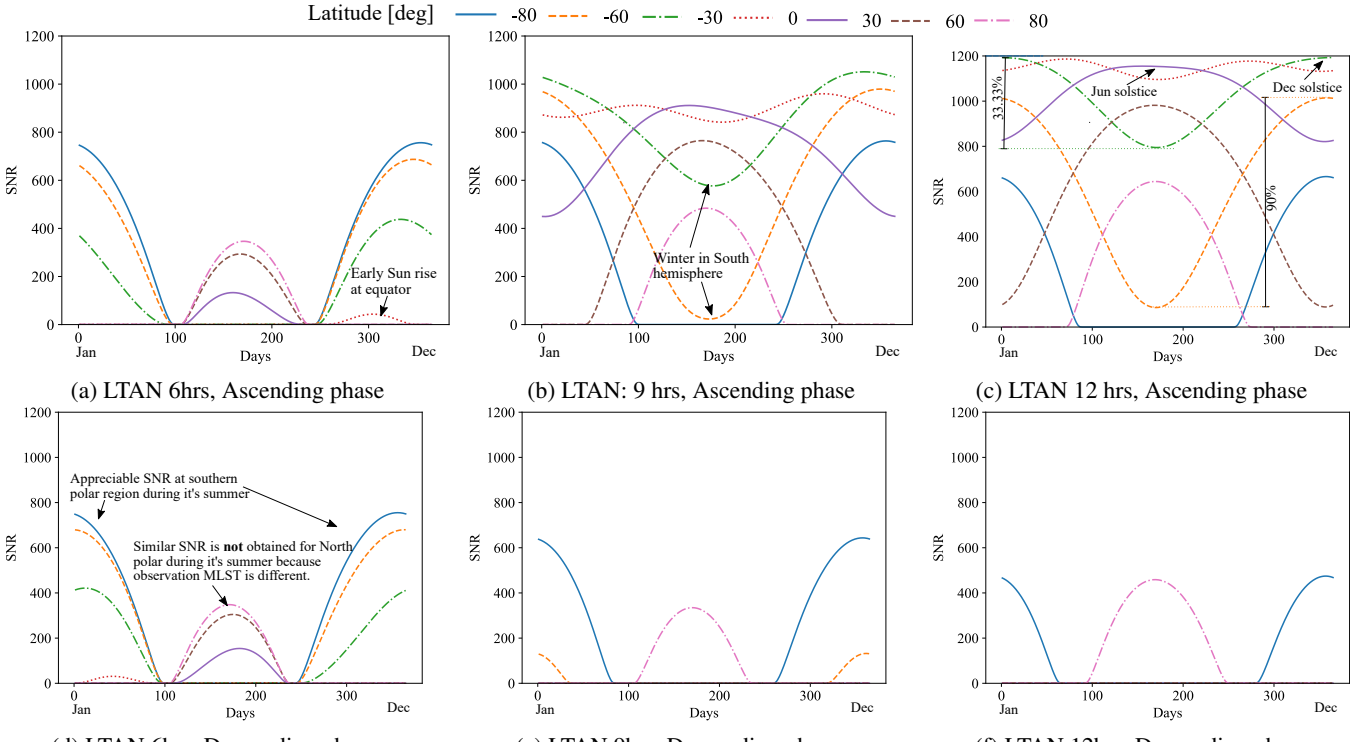

(a) LTAN 6hrs, Ascending phase

(b) LTAN: 9 hrs, Ascending phase

(c) LTAN 12 hrs, Ascending phase

(d) LTAN 6hrs, Descending phase

(e) LTAN 9hrs, Descending phase

(f) LTAN 12hrs, Descending phase

Figure 6: SNR plots as a function of days for the 894km altitude SSO at different LTANs, and different latitudes. The top three plots correspond to observation SNRs when the satellite ascends over the latitude, while the bottom three plots correspond to the satellite descent.

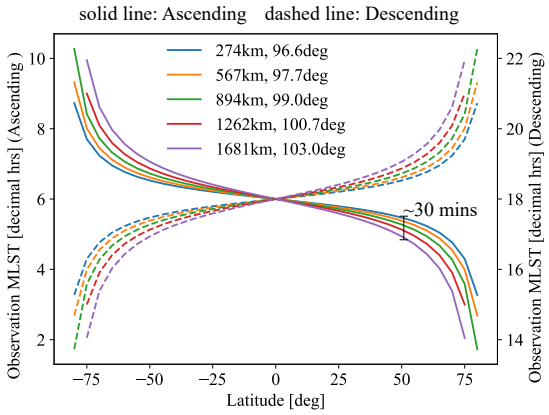

(a) LTAN: 6hrs

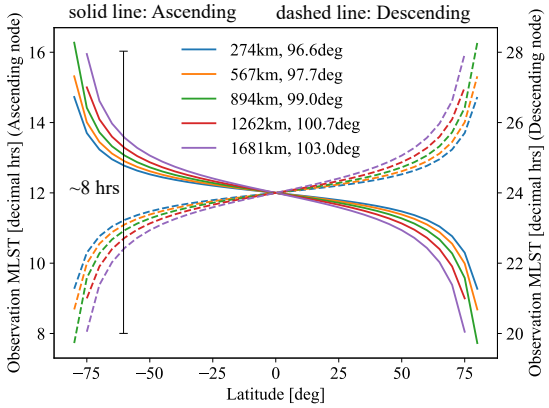

(b) LTAN: 12hrs

Figure 7: MLST (ascending and descending) during which observations are made, versus latitude for different SSOs at the same LTAN.

polar region) during the summer while during the winter no observations are possible. An intuitive way to visualize the position of the Sun at the same MLST of each day during a span of a year is terms of diagram called as the Analemma [35]. Drawing the Analemma at different times of the day we see that they in general have different shapes (different degrees of Sun elevation and azimuth angles) depending on the chosen MLST and latitude.

The variation in the true Sun position (true time) at different latitudes and at the same MLST at which observations take place by a satellite in a SSO orbit result in different Sun illuminations during the observations. Thus we expect variation in the observation SNR of a passive optical sensors imaging at Short-Wave Infra Red (SWIR), Near Infra Red (NIR), and Visible (VIS) spectral bands. To investigate this effect quantitatively, we use the instrument data-metrics evaluator to to evaluate the SNR for an instrument with parameters given by the OLI column in Table 1, for a global grid of ground points at 5^o latitude resolution (note that there is no longitudinal variation of the data-metrics), at each day over the course of one year. The observations are made by satellites at five different circular SSOs with altitudes: 274km, 567km, 894km, 1262km and 1681km corresponding to groundtrack repeat cycle of one day [34, Table 2]. Further for each SSO there are four different orbits corresponding to LTANs 6hrs, 9hrs, 12hrs and 15hrs (note that they also correspond to Local Time of Descending Node (LTDN) of 18hrs, 21hrs, 0hrs and 3 hrs, thus capture observations taken during an entire day at resolution of 3hrs). Thus we have in total a tradespace of 20 different orbits and one instrument evaluated over 1 year mission lifetime over 36 latitudes.

Variation in the SNR for fixed SSO altitude, different LTANs— We would first like to see the effect of choosing LTANs on the data-metrics. In Fig.6 the SNR corresponding to LTANs of 6hrs, 9hrs and 12hr at a 893km altitude SSO is plotted. While the top plots correspond to observations made at during the satellite ascent over the latitude, the bottom plots correspond to the observations during the descent of the satellite. A number of observations can be made from these plots:

- The variation of the SNR level increases as we go to higher latitudes from the equator. For example at LTAN of 12hrs, the SNR at the equator varies 1100 to 1200 (8.33%), the SNR for 30 deg latitudes is from 800 to 1200 (33.33%) and for 60 deg latitudes the SNR varies from 100 to 1000 (90%).
- The highest SNR levels at any given day is obtained at LTAN of 12 hrs which is reasonable considering that the *mean* Sun is directly overhead the equator and for other latitudes close to being overhead. However note that the highest level does not always happen at the equator. For example the highest level during June happens for the Tropic of Capricorn.
- Appreciable SNR levels exist at the polar regions during their respective summers over both the ascent and descent of the satellite. Further the polar SNR plots are roughly independent of the chosen LTAN.

Variation in the SNR for fixed LTAN, different SSOs— We would now like to see the behavior of the SNR metrics for different SSOs but at the same LTAN. The intuition in expecting any variation is because that different SSOs correspond to different inclinations, and the observation MLST at the latitudes shall be different even though it corresponds to the same LTAN as shown in Fig.7 where the MLST during both the ascent and descent of the satellite over the corresponding latitude is plotted. As can be expected the variation is zero at the equator since at the equator the observation MSLT = LTAN, and the variation starts to increase as the latitude increases. As an example comparing the 103deg inclined orbit and the 96.6deg inclined orbit, there is a difference of 30mins in the observation MLST for the 50deg latitude, 45mins for the 60 deg latitude and 1.5hrs for the 70deg latitude. Secondly we see that over all the cases the MLST roughly varies over a range of +/- 4 hours about the LTAN. For example, for an SSO with LTAN 12hrs, the southern most latitudes are images at 8hrs MLST, while the northern most latitudes are imaged at 16hrs MLST.

Figure 8 shows SNR statistics (mean, standard-deviation, median and # observations) corresponding to different SSOs at the same LTAN. The results of three different LTAN cases are shown: 9hrs, 12hrs and 15hrs. An SNR threshold of 200 is placed to mark an observation as "Valid" and the statistics are taken only for these samples. A "fair" comparison can be done for the SSOs at the higher altitudes since the integration time of the detector shall be the same for these cases and there is no gain in SNR with increasing altitude (more discussion about this behavior in Case 3). As expected, the standard-deviation is the lowest around and at the equatorial latitudes (regardless of the specific LTAN). There are sharp discontinuities at the higher latitudes, which is due to the application of SNR threshold value of 200 and because at the higher latitudes observations from the both the ascending and descending passes of the satellite start to yield valid observations (at lower latitudes only one of the passes shall yield valid observations). This is also reflected in the number of observations plot line where it is constant over the middle

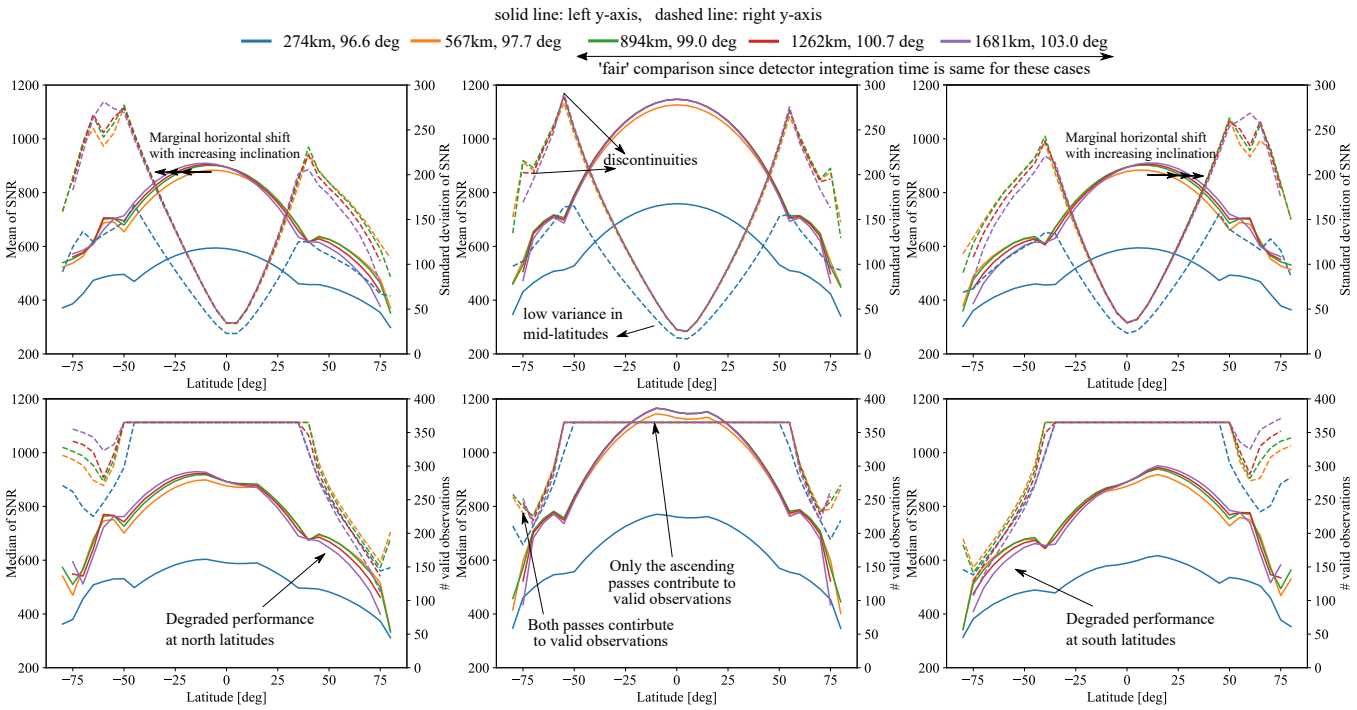

(a) LTAN: 9hrs (b) LTAN: 12hrs (c) LTAN: 15hrs

Figure 8: SNR statistics (mean, standard-deviation, median and # of observations) taken over SNR values over an entire year at different SSOs, versus latitude. An SNR threshold of 200 is considered. Each of the subplots corresponds to different LTANs. A "fair" comparison is possible for the 894km, 1262km and 1681km SSOs, since the integration time of the detector is the same, while for the 274km and 567km SSOs the integration time is less than the maximum specified value.

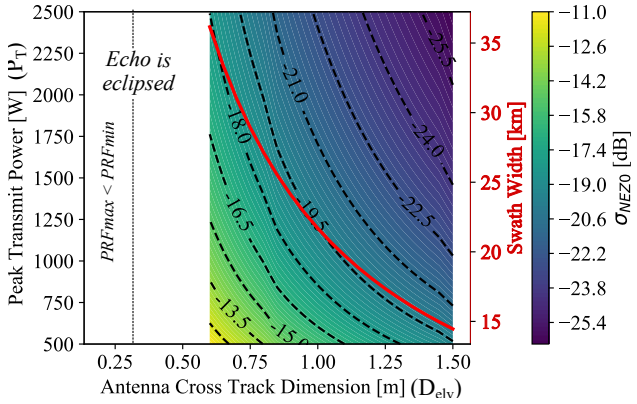

Figure 9: **Tradespace of SAR instrument parameters:** The nominal instrument parameters are off Table 3: MicroXSAR column. The antenna cross-track dimension (D_{elv}) and peak transmit power (P_T) are the tradespace parameters. Contour lines of constant σ_{NEZ0} are drawn and improve towards in the direction of top-right because of increasing P_T and antenna area. The swath-width (bold red plot line) decreases with the increase in D_{elv} (does not vary with P_T). The blank region corresponds to in-feasible region of operation.

latitudes, but starts to vary at the higher latitudes. Marginal skews and horizontal shifts in the plots lines are seen at the LTAN 9hrs and 15hrs (in opposite directions). For missions favoring observations in the northern latitudes ,LTAN greater than 12 hrs would be favorable.

Case 2

In this tradespace study example we consider the search-space of the instrument parameters for a given orbit and viewing geometry. Such a tradespace exploration is useful to find the most optimal instrument when the mission orbits have been decided. The example we consider is of a SAR instrument with nominal instrument parameters set to the values corresponding to the 'MicroXSAR X-band SAR' column in Table 3. We shall explore the tradespace of two of it's parameters: the SAR antenna cross-track dimension (D_{elv}) and the peak transmit power (P_T) while keeping the rest of the parameters at their nominal values. The f_P is set to the highest possible value within the $[f_P^{min}, f_P^{max}]$ satisfying all the PRF constraints.

Figure 9 shows the resulting σ_{NEZ0} of the tradespace. The σ_{NEZ0} improves with increasing D_{elv} and hence increasing antenna area, gain. It also improves with the increasing P_T. Increasing either of these parameters come with tradeoffs with the rest of the system. For example, increasing D_{elv} and hence the size of the instrument would increase the overall satellite size too. Increasing the peak transmit power level comes at the cost of increasing complexity and hence risk and is limited by the availability of corresponding high-power amplifier technology.

Also shown in Fig.9 the swath-width decreases with increase in D_{elv}. The antenna beamwidth (and hence FOV) is inversely proportional to the antenna dimension as seen in (28) and hence the illuminated swath-width. This would have negative effect on the coverage metrics, and is an example of the yin-yang of the data and coverage metrics.

A blank region corresponding to in-feasible SAR observa-

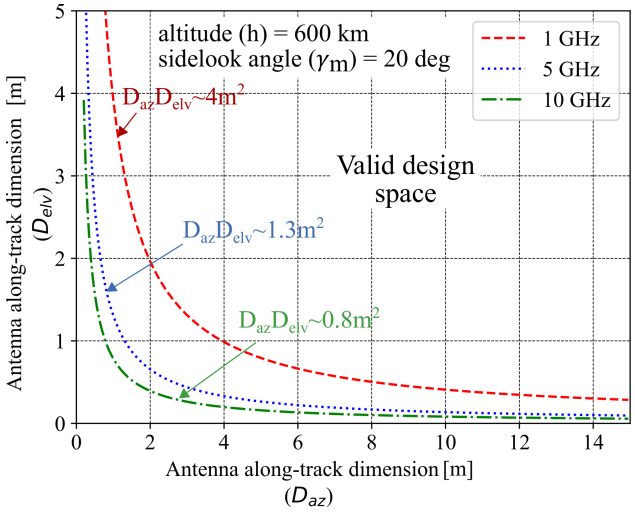

Figure 10: **Constraint on choosing SAR antenna dimensions:** Above plot is produced by equating the PRF_{min} and PRF_{max} and assuming the transmit pulse duration is negligible. The area in the concave side of the plot lines (with each line corresponding to a separate operational frequency) correspond to valid antenna dimensions which maybe used in the design of the SAR instrument. The plot was produced for observations for an altitude (h) of 600km and sidelook-angle (γ_m) of 20 deg. The required antenna area is seen to decrease with the increase in operating frequency.

tions appears for $D_{elv} < 0.6$m. For small D_{elv} the illuminated swath is larger and corresponds to an echo return of larger duration. This dictates the PRF_{max} which can be used (30). The Nyquist criteria applied for unambiguous Doppler detection which dictates the PRF_{min} given in (29) for the simulated case was 3618 Hz. For $D_{elv} < 0.3$m the calculated $PRF_{max} < PRF_{min}$ and hence observations are not possible. For $0.3\text{m} < D_{elv} < 0.6$m, the $PRF_{max} > PRF_{min}$, but other PRF constraints given in (31) and (32) render observations in-feasible. For $D_{elv} > 0.6$m the range of available PRF increases with the increasing PRF_{max} and thus observations are feasible.

The phenomenon of in-feasible regions of operation due to eclipsing of the return echo by transmit pulse is a characteristic of monostatic SAR. As seen in the above tradespace study it imposes indirectly an constraint on the antenna dimension. Let us consider only the outer bounds on the operable PRF, the PRF_{min} and PRF_{max} given in (29) and (30). While PRF_{min} is dictated by the along-track antenna length D_{az}, the PRF_{max} is dictated by D_{elv} (among other parameters). Since a valid PRF may exist only when $PRF_{min} < PRF_{max}$, it follows that not all combinations of D_{az}, D_{elv} maybe used for the SAR design. By equating (29) and (30) and assuming small transmit pulse lengths, Fig.10 was produced for different operational frequencies. The altitude $h = 600$km and mid-swath sidelook angle $\gamma_m = 20^o$ are the only other parameters whose values were assumed to produce the plots. The valid design space for selecting the SAR antenna dimensions falls in the concave side of the plot lines which appears to be hyperbolic. Indeed in [36] an analytical expression in the form of "minimum antenna area" (minimum $D_{az}D_{elv}$) required for SAR observation is derived with the assumption of imaging on a fictitious flat-Earth surface. It should be noted that for the case of "in-feasible observations", observations maybe made by relaxing the PRF_{max} condition by making observation of only the non-eclipsed part of the return echo (corresponding to a smaller swath) or by relaxing the PRF_{min} condition by allowing for coarser azimuthal resolution (also suggested in [36]). However this comes at a cost, for example in the case of ignoring the eclipsed part of the echo, we operate inefficiently in terms of power because there is wastage of the energy spent in illuminating the swath corresponding to the eclipsed part of the echo.

Case 3

In [11, Table 9-10] a qualitative comparison between the different scanning technologies for passive optical sensors is given. In this section we use the data metric evaluator to quantitatively compare the tradeoffs between two of the scanning technologies: pushbroom and whiskbroom. To get a preliminary idea of the two technologies we may look at Table 1 and compare values of the instrument parameters of the OLI (pushbroom) and MODIS (whiskbroom) (which are tabled at nearly the same operating wavelength). While the number of detectors of the pushbroom sensors is in 1000s, the number of detector for MODIS is 10. The integration time for MODIS is about 10 times less. The aperture diameter of MODIS is relatively larger, but the focal length is relatively smaller. While the pushbroom sensor has a modest 15 deg cross-track FOV, MODIS has 110 deg cross-track FOV and hence can image a larger swath. The resulting data-metrics of the instruments are SNR: 802 for MODIS (Band10) vs 367 for OLI (Blue band) and 1000m pixel resolution for MODIS (Band10) vs 30m for OLI [20] [19]. While MODIS seems to enjoy a wide swath, fewer number of detectors, greater spectral resolution and larger SNR, it is coming at the cost of an increased aperture diameter and much coarser pixel resolutions.

For this case study we select the nominal (reference) instrument specifications as that of the "Firesat" whiskbroom thermal imager (hereby referred to as WBX) given in [11, Table 9-15]. A corresponding nominal pushbroom sensor

Table 5: Case 3 nominal specifications of the test instruments under study. Please refer to Table 1 for description of the symbols.

Instrument parameter)	**WBX**	**PBX**
Orientation	Nadir-looking	Nadir-looking
$\theta_{AT} \times \theta_{CT}$	0.628°x115.8°	0.628°x115.8°
Scan technique [2]	Whisk-broom	Push-broom
$N_d^{AT} \times N_d^{CT}$	256x1	1x47158
$F\#$	2.7	2.7
f	0.7m	0.7m
λ_0	4.2um	4.2um
$\Delta\lambda$	1.9um	1.9um
c_e	50%	50%
T	290K	290K
τ_{op}	75%	75%
Bits per pixel	8	8
d	30um	30um
D_{ap}	0.26m	0.26m
T_i^{max}	unrestricted	unrestricted
N_r	25	25

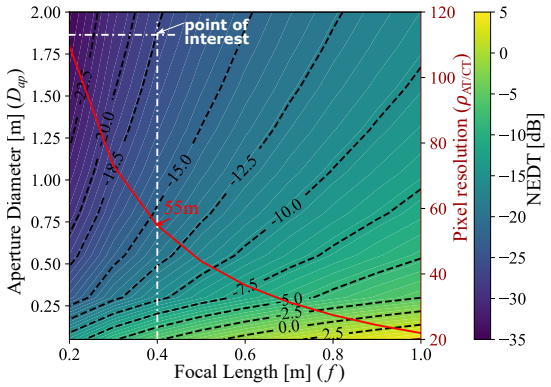

(a) Whiskbroom WBX NEDT contours

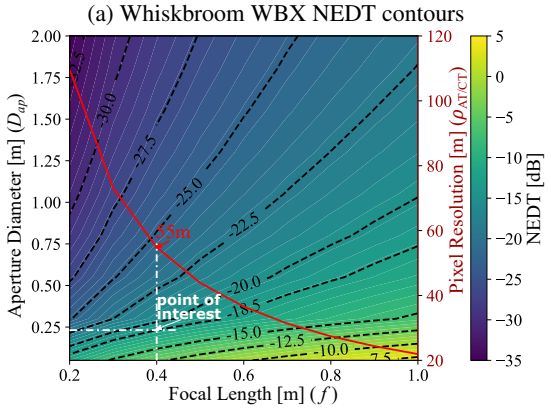

(b) Pushbroom WBX NEDT contours

Figure 11: Tradespace of focal-length (f) vs aperture diameter (D_{ap}) for the whiskroom WBX and pushbroom PBX instruments showing the NEDT contours and pixel resolution plot line. The SNR contours (not shown) follow the same trend as the NEDT contours. The expression in decibels is made considering reference NEDT as 1 Kelvin.

specifications (hereby referred to as PBX) is made by selecting the number of detectors in the cross-track direction to give the same cross-track FOV as its whiskbroom counterpart. The specifications are listed in Table 5. The target geometry considered in all the analysis of this section was imaging from an altitude of 700km at a pixel in the nadir direction with unity surface reflectivity.

In the first scenario we explore the effect on the data-metrics by variation in the aperture diameter and focal length for both the instruments, and we see under what conditions both the sensors yield similar data metrics. In this scenario we do not restrict the integration time of the detectors, i.e. we let the integration time equal to the access duration (see (11)). Figure 11 plots the results showing the NEDT and pixel resolutions. It must be noted that by varying the focal-length and aperture diameter other instrument parameters too are varied due to the constraint relation (see (8)). For example, increasing the focal-length decreases the IFOV of the detectors and hence also the pixel resolutions (along-track and cross-track) as shown in the red plot line. Both the SNR and NEDT follow the same trend, i.e. they improve moving towards the direction of increasing aperture diameter and decreasing focal length. The decrease in focal length increases the pixel area over which radiated/ reflected electromagnetic energy is collected and hence improves the radiometric resolution (but degrades the spatial resolution). For the same optical specifications, and an unrestricted sensor integration time, the pushbroom sensor yields far greater data-metrics compared to the whishbroom counterpart. Focusing on the labeled "point of interest", a whiskbroom sensor with 1.88m aperture diameter is seen to give the same data-metrics (NEDT and pixel resolutions) as that of a pushbroom sensor with 0.25m aperture-diameter.

The SNR gain obtained by pushbroom sensors is due to the increased integration-time for each detector. However, in practice this increase in the integration time has a limitation depending on the detector and its accompanying electronics. In the instrument parameters outlined in the Table 1 this effect is taken into consideration by the T_i^{max} parameter. A large T_i^{max} is desirable since it implies a larger number of signal electrons can be collected by the detector, and this is turn translates to an higher dynamic range.

Consider the tradespace of altitude and aperture-diameter shown in Fig.12 for pushbroom and whiskbroom sensors. As the altitude increases, for a given IFOV the access duration increases. Suppose we were working with detectors with large T_i^{max} (Fig.12c) the SNR data metric is seen to increase with increasing altitude for the whiskbroom sensor. However for the pushbroom sensor the T_i^{max} has become the limiting factor at lower altitudes itself and hence the SNR stays constant (characteristic of the assumed Lambertian surface model). For the case of whiskbroom sensor, the limit is reached at altitudes 600km, 1300km and 2150km for T_i^{max}= 20μs, 50μs and 100μs respectively. These may be termed as the "threshold" altitudes (for the corresponding maximum integration times) at which the performance of the whiskbroom sensor (in terms of SNR and pixel resolution) matches that off the pushbroom sensor. Thus, for mission orbits above these threshold altitudes, one may find it more desirable to use whiskbroom sensors given their high uniformity in the entire scene response due to use of smaller number of pixels.

Before we conclude this section, we would caution that strictly speaking T_i^{max} is not independent of the other instrument parameters. More fundamentally the limits of the detector are due to a finite signal electron collection capacity (eg: full-well capacity in CMOS and CCD imagers). Consider the contours of the number of maximum signal electrons drawn in Fig.13 against the instrument parameters bandwidth and aperture diameter for the PBX sensor. To get an estimate of the *maximum* number of the signal electrons, a target temperature of 700K (example of the highest temperature expected to be imaged by the instrument) was considered. The number of signal electrons grows rapidly with the increase in both the instrument parameters. The growth with the increase in bandwidth appears to saturate at higher bandwidths, the reason for which is attributed to the role played by the atmospheric transmittance over the bandwidth of interest (shown in Fig.13b). We may thus expect the required T_i^{max} to also grow similarly.

7. SUMMARY

In this paper we have described the concept, framework and implementation of an instrument data metrics evaluator geared towards analysis of Pre-phase A satellite missions. A numerical point data-metrics evaluation approach was adopted in the framework against an approximate analytic approach to accommodate all types of mission scenarios. There are several subtle issues which rise in the process of adopting this framework, such as what values should be considered for the operational parameters, how to model

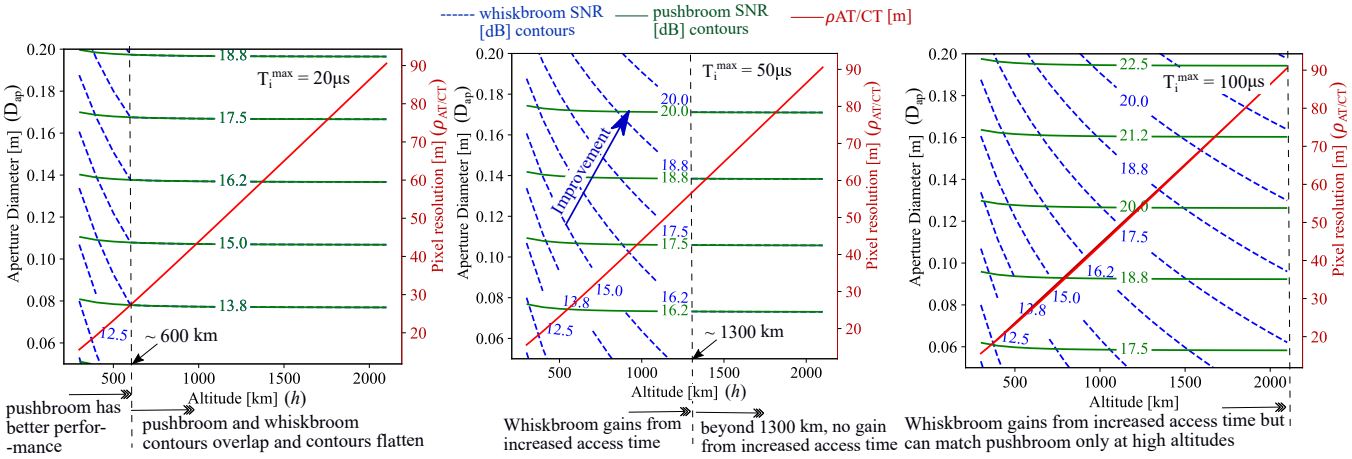

(a) 20μs maximum integration time (b) 50μs maximum integration time (c) 100μs maximum integration time

Figure 12: SNR [dB] contours and pixel resolution plots of pushbroom (PBS) and whiskbroom (WBX) sensors for different maximum integration times in the tradespace of altitude and aperture diameter. The expression of SNR in decibels is made considering reference SNR as 1.

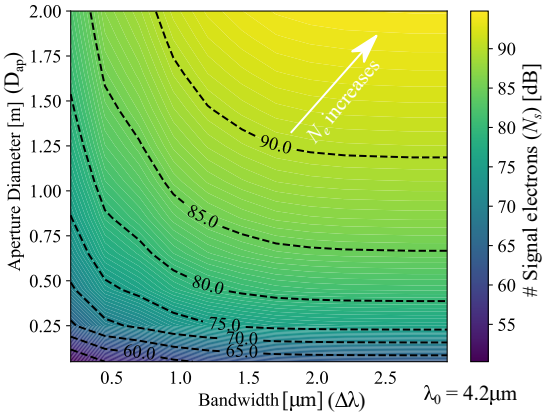

(a) Contours of number of signal electrons [dB] in the tradespace of bandwidth and aperture diameter. The expression in decibels is made considering reference number of signal electron as 1.

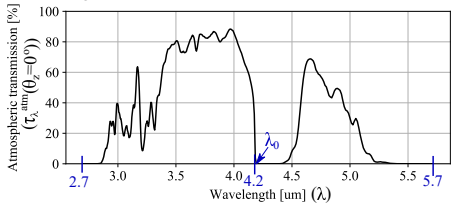

(b) Atmospheric transmission in bandwidth of interest.

Figure 13: Signal electrons captured over an fixed integration time of 100μs and target black body temperature of 700K.

highly complex real-world instruments for which hardware data may not be available in open literature, etc. Reasonable assumptions were made to circumvent these issues.

Then we considered instrument modeling of different instrument classes, where we began with an *basic sensor* class which essentially produces the target viewing geometry parameters as the evaluated data-metrics. Such a model maybe used for cases when there is little available information about an instrument. The second class we considered was the *passive optical sensor* which can be used to model passive instruments operating at and near optical wavelengths. The class also allows for definition of different scanning techniques: pushbroom, whiskbroom and matrix. The last instrument class presented was the *synthetic aperture radar*. Real world instruments were surveyed and their equivalent parameters for the presented models was tabled.

Finally we utilized the described data-metric evaluator and obtained unique results for some important mission design use-cases. In case of SSOs we were able to quantify the variation in the SNR over the course of an year of mission at different latitudes. The variation in the SNR for SSOs at different altitudes but with the same LTAN too was analyzed. The second use-case involved SAR, and considered the tradespace of the antenna size and transmit peak power. The influence of the PRF constraints was highlighted and a fundamental constraint in the minimum required size of the antenna is shown. The last use-case considered the tradespace of pushbroom and whiskbroom sensors. Two different scenarios, one involving unrestricted detector integration time and other with specified maximum detector integration times was considered. Examples of design points at which both the technologies yield identical data-metrics was shown.

APPENDICES

A. PRF CONSTRAINT DUE TO NADIR ECHOS IN SAR IMAGING

Consider the SAR imaging geometry in Fig.5 and the definitions of $h, R_e, R_n, R_f, \tau_n, \tau_f, \tau_{nadir}$ be the same as in Section.5. Let $T = 1/f_P$ is the time-period corresponding to pulse-repetition-frequency f_P at which the observation is made. The nadir echo from the pulse (hereby referred to as the reference pulse) whose desired echo (from the desired swath) we sample can occur due to echos from the reference pulse and pulses occurring after the reference pulse.

Interference from nadir echo of reference (1st) pulse

Consider the timing diagram of the nadir echo and the desired echo shown in Fig.14. The nadir echo occurs before the desired echo due to the shorter range corresponding to the

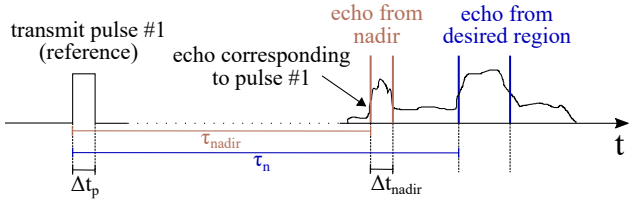

Figure 14: Timing diagram to calculate non-interference condition from nadir echo of reference pulse.

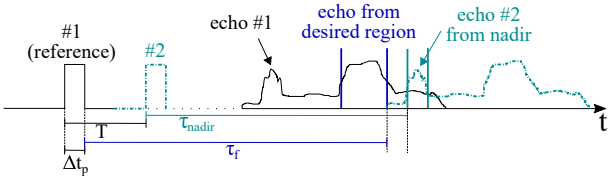

(a) Nadir echo of the second transmit pulse occurs *after* the desired echo.

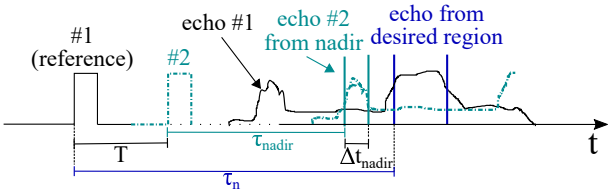

(b) Nadir echo of the second transmit pulse occurs *before* the desired echo.

Figure 15: Timing diagram to calculate non-interference condition from nadir echo of second transmit pulse.

nadir direction. We can write the condition so that there is *no* interference as:

$$\tau_n > \tau_{nadir} + \Delta t_{nadir}$$

$$\frac{2R_n}{c} > \frac{2h}{c} + \Delta t_{nadir} \tag{36}$$

It may be noted that this condition is independent of f_P. Further, note that when interference with beginning of desired echo window is to be considered, the desired echo starts at the point when the *first reflections* from the near range swath reach radar receiver. Hence τ_n is measured from the *rising edge* of transmit pulse. When interference with end of desired echo window is to be considered, the desired echo ends at the point when the *last reflections* from the far range swath reach radar receiver. Hence τ_f is measured from the *falling edge* of transmit pulse.

Interference from nadir echo from next (2nd) transmit pulse

The nadir echo from the 2nd transmit pulse has to reside either after or before the desired echo do that it does not interfere. We find each of these conditions separately as follows:

Nadir echo after desired echo window— From the timing diagram shown in Fig.15a:

$$\tau_{nadir} > \tau_f + \Delta t_p - T$$

$$=> f_P < \frac{1}{\frac{2R_f}{c} + \Delta t_p - \frac{2h}{c}} \tag{37}$$

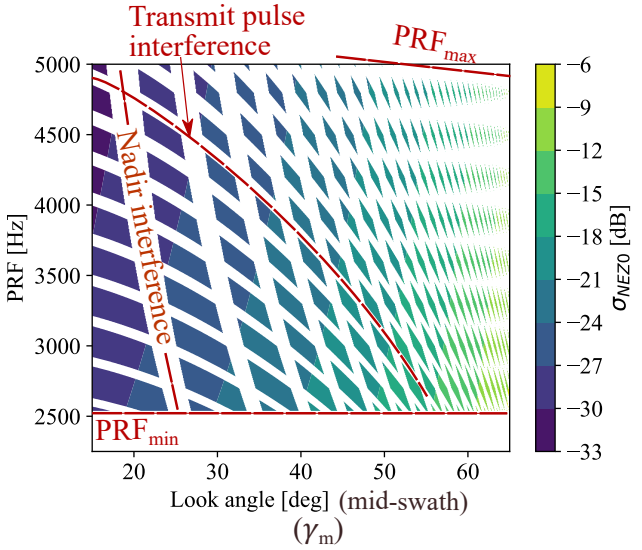

Figure 16: **Tradespace plot of look angle vs PRF highlighting the PRF constraints.** Simulated system parameters: Altitude=500km, Velocity=7613ms, Antenna Length= 6.0m, Tx Pulse Length= 30.0us, Swath Width=10km. Compare with [30, Fig.5.1.14.1].

Nadir echo before desired echo window—From the timing diagram shown in Fig.15b:

$$\tau_n > \tau_{nadir} + \Delta t_{nadir} + T$$

$$=> f_P > \frac{1}{\frac{2R_2}{c} - \frac{2h}{c} - \Delta t_{nadir}} \tag{38}$$

Note that either (37) **or** (38) needs to be satisfied so that there is no nadir interference.

Generalizing for the case of no interference for the m^{th} successive transmit pulse

In general the nadir echo from 3rd or 4th ..... transmit pulses may interfere with the desired echo window of the 1st transmit pulse. We can generalize (36), (37) and (38) and write the condition for no interference from the j^{th} pulse as:

$$f_P < \frac{m}{\frac{2R_f}{c} + \Delta t_p - \frac{2h}{c}} \quad (or) \quad f_P > \frac{m}{\frac{2R_n}{c} - \frac{2h}{c} - \Delta t_{nadir}} \tag{39}$$

where $m = 1, 2, ..., M$ and $M = int(f_P \frac{2R_f}{c}) + 1$ is the transmit pulse number after the desired echo has ended. The condition may be also expressed as:

$$f_P \notin \left[\frac{m}{\frac{2R_n}{c} - \frac{2h}{c} - \Delta t_{nadir}}, \frac{m}{\frac{2R_f}{c} + \Delta t_p - \frac{2h}{c}} \right] \tag{40}$$

For small antenna beamwidth at the nadir direction it can be shown that the duration of the nadir echo Δt_{nadir} is approximately same as the transmit pulse length, i.e. $\Delta t_{nadir} \approx \Delta t_p$.

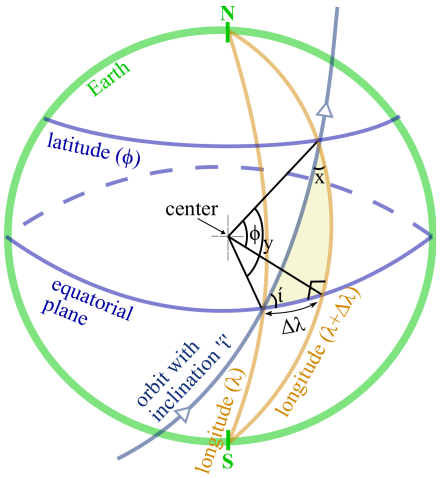

Figure 17: Illustration accompanying derivation of the calculation of local time of satellite passes over a latitude given the orbit LTAN.

Comparing (40) with the corresponding inequality in [30, 5.1.5.2], we see that the they are complimentary. In this derivation we have shown that the correct condition is (40). Figure 16 shows the tradespace corresponding to varying PRF and instrument side-look angle. Lower and upper bounds corresponding to PRF_{min}, PRF_{max} are shown. The blank regions within the bounds correspond to the interference by either the transmit pulse or nadir echos. The simulation parameters were the same as those used in [30, Fig.5.1.14.1]. The results of the interference of both the tradespace plots match, which indicate that the nadir-interference inequality [30, 5.1.5.2] might have been printed wrongly.

B. Local time for satellite passes over a given latitude at a specified LTAN

This section describes the calculation of the local time at which a satellite in a SSO, ascends and descends over a given latitude, given the LTAN. Consider an orbit with inclination i as shown in Fig.17, passing the equator at longitude λ. Let the LTAN of the orbit be t_0 which by definition of LTAN is the time at which the satellite passes over the equator. We shall calculate the local (Solar mean) time of ascent and descent of the satellite across the latitude ϕ.

In Fig.17 consider the spherical triangle subtended by the angles ϕ (latitude), $\Delta\lambda$ (unknown longitude difference between the ascending node on the equator and ascending node on latitude ϕ) and y (unknown). The angles formed by the triangle are: 90^o (between the equatorial plane and longitude $\lambda + \Delta\lambda$ plane), x (unknown, between the orbit plane and longitude $\lambda + \Delta\lambda$ plane) and i (inclination of orbit plane). Using the spherical law of sines and cosines:

$$\frac{\sin i}{\sin \phi} = \frac{\sin x}{\sin \Delta\lambda} = \frac{1}{\sin y}$$
$$\cos y = \cos\phi \cos \Delta\lambda$$

Above equations are solved to find $\Delta\lambda$ and the sign is adjusted so that:

$$\Delta\lambda = \begin{cases} -|\Delta\lambda|, & \text{if } i \geq 90^o \ \& \ \phi \geq 0^o \\ -|\Delta\lambda|, & \text{if } i < 90^o \ \& \ \phi < 0^o \\ +|\Delta\lambda|, & \text{otherwise} \end{cases}$$

The local time of ascent (t_{asc}) and descent (t_{dsc}) (in decimal hours) at latitude ϕ are:

$$t_{asc} = t_0 + \Delta\lambda \frac{24}{360}$$
$$t_{dsc} = t_0 - \Delta\lambda \frac{24}{360} + 12$$

Acknowledgments

This research is supported by the project "Generalizing Distributed Missions Design Using the TradeSpace Analysis Tool for Constellations and Machine Learning" (NASA Grant Number: 80NSSC17K0572).

References

[1] J. Mason, I. Zuleta, and J. Mascaro, "Remote sensing with disaggregated cubesat constellations," in *NASA Earth Science Technology Forum*, Junes 2019.

[2] T. Obata, H. Saito, K. Tanaka, S. Nakasuka, and S. Shirasaka, "The development status of the first demonstration satellite of our commercial small synthetic aperture radar satellite constellation," 2019.

[3] I. del Portillo, B. G. Cameron, and E. F. Crawley, "A technical comparison of three low earth orbit satellite constellation systems to provide global broadband," *Acta Astronautica*, vol. 159, pp. 123–135, 2019.

[4] J. Le Moigne, P. Dabney, O. de Weck, V. Foreman, P. Grogan, M. Holland, S. Hughes, and S. Nag, "Tradespace analysis tool for designing constellations (TAT-C)," in *2017 IEEE International Geoscience and Remote Sensing Symposium (IGARSS)*, July 2017, pp. 1181–1184.

[5] S. Nag, S. P. Hughes, and J. J. LeMoigne, "Navigating the deployment and downlink tradespace for earth imaging constellations," 2017.

[6] S. Nag, S. P. Hughes, and J. Le Moigne, "Streamlining the design tradespace for earth imaging constellations," in *AIAA SPACE 2016*, 2016, p. 5561.

[7] P. G. Buzzi, D. Selva, N. Hitomi, and W. J. Blackwell, "Assessment of constellation designs for earth observation: Application to the tropics mission," *Acta Astronautica*, vol. 161, pp. 166–182, 2019.

[8] T. Savitri, Y. Kim, S. Jo, and H. Bang, "Satellite constellation orbit design optimization with combined genetic algorithm and semianalytical approach," *International Journal of Aerospace Engineering*, vol. 2017, 2017.

[9] S. W. Paek, S. Kim, and O. de Weck, "Optimization of reconfigurable satellite constellations using simulated annealing and genetic algorithm," *Sensors*, vol. 19, no. 4, p. 765, 2019.

[10] S. Nag, V. Ravindra, and J. L. Moigne, "Instrument modeling concepts for tradespace analysis of satellite constellations," in *2018 IEEE SENSORS*, Oct 2018, pp. 1–4.

[11] J. Wertz and W. J. Larson, *Space Mission Analysis and Design*, 3rd ed. Springer Netherlands, 1999.

[12] V. Ravindra and S. Nag, "Fast methods of coverage evaluation for tradespace analysis of constellations," *IEEE Journal of Selected Topics in Applied Earth Observations and Remote Sensing*, 2020, submitted.

[13] E. Knight and G. Kvaran, "Landsat-8 operational land imager design, characterization and performance," *Remote Sensing*, vol. 6, no. 11, pp. 10 286–10 305, 2014.

[14] D. Reuter *et al.*, "The thermal infrared sensor (TIRS) on landsat 8: Design overview and pre-launch characterization," *Remote Sensing*, vol. 7, no. 1, pp. 1135–1153, jan 2015.

[15] M. S. Grewal, L. R. Weill, and A. P. Andrews, *Global positioning systems, inertial navigation, and integration*. John Wiley & Sons, 2007.

[16] D. A. Vallado, *Fundamentals of astrodynamics and applications*. Springer Science & Business Media, 2001, vol. 12.

[17] T. Arvidson, J. Barsi, M. Jhabvala, and D. Reuter, "Landsat and thermal infrared imaging," in *Thermal Infrared Remote Sensing*. Springer, 2013, pp. 177–196.

[18] "Landsat-8 / LDCM (landsat data continuity mission)," accessed: 2019-09-14. [Online]. Available: https://earth.esa.int/web/eoportal/satellite-missions/l/landsat-8-ldcm

[19] R. Morfitt, J. Barsi, R. Levy, B. Markham, E. Micijevic, L. Ong, P. Scaramuzza, and K. Vanderwerff, "Landsat-8 operational land imager (OLI) radiometric performance on-orbit," *Remote Sensing*, vol. 7, no. 2, pp. 2208–2237, feb 2015.

[20] "MODIS: Moderate resolution imaging spectroradiometer)," accessed: 2019-09-14. [Online]. Available: https://modis.gsfc.nasa.gov/about/

[21] W. L. Barnes, T. S. Pagano, and V. V. Salomonson, "Prelaunch characteristics of the moderate resolution imaging spectroradiometer (MODIS) on EOS-AM1," *IEEE Transactions on Geoscience and Remote Sensing*, vol. 36, no. 4, pp. 1088–1100, 1998.

[22] M. Nishihama, "MODIS level 1A Earth location: Algorithm theoretical basis document version 3.0," Aug 1997.

[23] W. L. Barnes and V. V. Salomonson, "MODIS: A global imaging spectroradiometer for the earth observing system," in *Optical Technologies for Aerospace Sensing: A Critical Review*, vol. 10269. International Society for Optics and Photonics, 1992.

[24] E. Allthorpe-Mullis *et al.*, "Cubesat camera: A low cost imaging system for cubesat platforms," in *7th Interplanetary CubeSat Workshop*, 2018.

[25] F. X. Kneizys, E. Shettle, L. Abreu, J. H. Chetwynd, and G. P. Anderson, "Users guide to LOWTRAN 7," Air Force Geophysics Lab Hanscom AFB MA, Tech. Rep., 1988.

[26] M. Hirsch, "Model of earth atmosphere absorption and transmission vs. wavelength and location." 2019, accessed: 2019-09-14. [Online]. Available: https://pypi.org/project/lowtran/

[27] K. Tomiyasu, "Tutorial review of synthetic-aperture radar (sar) with applications to imaging of the ocean surface," *Proceedings of the IEEE*, vol. 66, no. 5, pp. 563–583, 1978.

[28] A. Moreira, P. Prats-Iraola, M. Younis, G. Krieger, I. Hajnsek, and K. P. Papathanassiou, "A tutorial on synthetic aperture radar," *IEEE Geoscience and remote sensing magazine*, vol. 1, no. 1, pp. 6–43, 2013.

[29] A. W. Doerry, "Performance limits for synthetic aperture radar," Sandia National Laboratories Albuquerque NM, Tech. Rep., 2006.

[30] D. Bickel, B. Brock, and C. Allen, *Spaceborne SAR study: LDRD 92 final report*, Mar 1993.

[31] R. L. Jordan, "The Seasat-A synthetic aperture radar system," *IEEE Journal of Oceanic Engineering*, vol. 5, no. 2, pp. 154–164, 1980.

[32] H. Saito *et al.*, "Compact x-band synthetic aperture radar for 100kg class satellite," *IEICE Transactions on Communications*, vol. E100.B, no. 9, pp. 1653–1660, 2017.

[33] C. Elachi, T. Bicknell, R. Jordan, and C. Wu, "Spaceborne synthetic-aperture imaging radars: Applications, techniques, and technology," *Proceedings of the IEEE*, vol. 70, no. 10, pp. 1174–1209, 1982.

[34] R. J. Boain, "AB-Cs of sun-synchronous orbit mission design," 2004.

[35] P. Lynch, "The equation of time and the analemma," *Bull. Irish Math. Soc*, vol. 69, pp. 47–56, 2012.

[36] A. Freeman, W. T. Johnson, B. Huneycutt, R. Jordan, S. Hensley, P. Siqueira, and J. Curlander, "The "myth" of the minimum sar antenna area constraint," *IEEE Transactions on Geoscience and Remote Sensing*, vol. 38, no. 1, pp. 320–324, 2000.

BIOGRAPHY

Dr. Vinay Ravindra *is a Research Scientist at NASA Goddard Space Flight Center and NASA Ames Research Center (contracted by Bay Area Environmental Research Institute). He received his PhD in Electrical Engineering and Information Systems from the University of Tokyo. His research interests are small satellite systems, passive microwave devices, attitude determination and control of satellites and mission design.*

Dr. Sreeja Nag *is a Senior Research Scientist at NASA Goddard Space Flight Center and NASA Ames Research Center (contracted by Bay Area Environmental Research Institute). She completed her PhD in Space Systems Engineering from the Department of Aeronautics and Astronautics at Massachusetts Institute of Technology. Her research interests include distributed space systems, automated planning and scheduling of constellations, swarm decision making in space, and space traffic management.*